

# A Framework for Statistical Geometric Channel Model for ISAC Systems

Ali Waqar Azim, Ahmad Bazzi, Theodore S. Rappaport, Marwa Chafii

**Abstract**—This paper proposes a comprehensive framework for a geometry-based statistical model for integrated sensing and communication (ISAC) tailored for bistatic systems. Our dual-component model decomposes the ISAC channel into a target channel encompassing all multipath components produced by a sensing target parameterized by the target's radar cross-section and scattering points, and a background channel comprising all other propagation paths that do not interact with the sensing target. The framework extends TR38.901 via a hybrid clustering approach, integrating spatiotemporally consistent deterministic clusters with stochastic clusters to preserve channel reciprocity and absolute delay alignment for sensing parameter estimation. Extensive simulations across urban macro, urban micro, and indoor factory scenarios demonstrate that the model maintains communication performance parity with the standard TR38.901, validated through bit-error rate analysis obtained via simulated and measured ISAC channels and channel capacity assessment, while enabling sensing performance evaluation, such as target ranging error for localization and receiver operating characteristic curves for detection probability.

**Index Terms**—Integrated Sensing and Communication, Geometry-Based Stochastic Channel Model, Bistatic Sensing, Radar Cross-Section.

## I. INTRODUCTION

Integrated sensing and communications (ISAC) is a transformative paradigm for 6G systems, enabling joint sensing and communication functionalities through shared resources [1]. This resource sharing requires a unified channel model that supports reliable communication and accurate sensing. Unlike conventional communication channels, the ISAC channel must jointly model two components: (1) the *background channel* representing propagation independent of sensing targets, and (2) the *target channel* representing reflections from sensing targets [2]. Target-induced returns manifest as additional resolvable paths in the channel impulse response (CIR), with time-varying complex amplitudes and associated Doppler shifts.

Current standardized legacy geometry-based stochastic model (GBSM) channel models, such as 3rd Generation Partnership Project (3GPP) technical report (TR)38.901 [3], are fundamentally limited for ISAC applications. These models characterize propagation through statistical clusters and stochastically defined interaction processes, thereby lacking explicit, geometrically consistent scatterer representation needed for sensing. Furthermore, this statistical approach also neglects critical target-specific features and phenomenology, such as radar cross-section (RCS) and associated Doppler spreads. Although site-specific ray-tracing can implicitly capture target-channel interactions, its prohibitive computational

complexity precludes large-scale system simulation. Recognizing this gap, 3GPP has introduced new study items in Release 19 dedicated to ISAC channel modeling (CM) [4]. The resulting CM framework must therefore be architected around a unified representation of the target and background channels. This requires a shift from purely stochastic cluster modeling to a hybrid approach where environmental objects (EOs) are represented deterministically, defined by parameters such as 3D position, orientation, and velocity, while inherently supporting spatiotemporal consistency, extended object representation, and channel reciprocity [5]. Here, spatiotemporal consistency is defined as the property where scattering clusters possess pre-defined locations and deterministic reflection properties.

### A. Evolution of 3GPP Geometric Stochastic Channel Models

The development of TR38.901 [3] results from steady advancements in communication systems, where the progression began with the spatial channel model (SCM) in TR25.996 for 3G/UMTS, which introduced a geometric stochastic approach limited to 2D spatial propagation in the azimuth plane [6]. LTE systems further necessitated elevation modeling, leading to the 3D channel model in TR36.873 [7], which then extended the SCM framework to 3D space by incorporating zenith angles of arrival (AA) and angles of departure (AD), creating a full 3D spatial channel framework. TR38.901 [3] is the consolidation of these prior models. It inherits stochastic frameworks from TR36.873 and extends it to support higher frequency bands (up to 100 GHz), a wider range of deployment scenarios, and more detailed parameterization. However, despite its sophistication for communication-centric simulations, its core approach remains based on the statistical characterization of propagation clusters, which poses inherent limitations for ISAC and as such, cannot be used for ISAC system evaluation. The proposed sensing channel representation can also support network-level decisions in emerging integrated access and backhaul (IAB) architectures. More specifically, the network can identify locations that support high-throughput, relatively unobstructed wireless backhaul links at millimeter wave bands, and distinguish them from regions where the channel is poorly suited for wireless backhaul and alternative (e.g., wired or out-of-band) solutions are preferable, which creates a provisioning mechanism whereby the same ISAC framework used for radio environment sensing can guide IAB planning and dynamic backhaul selection, complementing early work on IAB at millimeter wave frequencies [8].

### B. Related Work

Recent advances in ISAC systems have spurred significant progress in ISAC CM, addressing its unique challenges. Different scatterer-based hybrid models have been proposed, combining deterministic and stochastic components for improved

Ali Waqar Azim Ahmad Bazzi, and Marwa Chafii are with the Engineering Division, New York University (NYU) Abu Dhabi, 129188, UAE (email: ali.waqar.azim,ahmad.bazzi,marwa.chafii@nyu.edu). Ahmad Bazzi, Theodore S. Rappaport, and Marwa Chafii are with NYU WIRELESS, NYU Tandon School of Engineering, Brooklyn, 11201, NY, USA .

accuracy, such as [9]. Further developments include extensions to GBSM, incorporating localization-assisted features [10] and unified representations of communication and sensing channels [11]. [10] integrates forward and backward scattering to enhance modeling fidelity. For bistatic ISAC systems, recent frameworks introduce weak-power cluster retention for target characterization [12]. Furthermore, cluster-based ISAC CM framework in [13] decomposes the environment into line-of-sight (LoS), non line-of-sight (NLoS), and clutter components, whose weighted summation yields the effective CIR, effectively integrating sensing characteristics into communication models. [14] introduces a 3GPP-compliant GBSM to support ISAC by introducing sharing feature that enables flexible modeling of shared clusters, scatterers, and propagation paths across communication and sensing channels within a unified stochastic framework. [15] presents a shared multipath component evolution model to characterize the correlation between communication and sensing channels in ISAC, validated through 28 GHz measurements. Hybrid methodologies combining statistical and deterministic techniques have also emerged, leveraging multi-scattering center models for precise target characterization [16]. Beyond physical-layer modeling, recent surveys highlight features such as RCS integration and artificial intelligence (AI)-enhanced frameworks for sub-6 GHz/mmWave bands [17]. In this context, NYURay [18], a site-specific 3D ray tracer developed at NYU WIRELESS, can be used for ISAC [19] owing to its site-specific ray tracing with the very same angular and temporal parameters a sensing algorithm will use, while NYUSIM [20] can provide statistical insights because of the stochastic channel and can be useful for large-scale simulation studies requiring system- or link-level testing, beamforming evaluation, and statistical coverage/capacity analysis. Recent work has demonstrated that NYURay can be pushed to the mobile or edge to perform multi-stage location optimization by aligning measured and simulated power-delay profiles and to calibrate and validate the NYURay simulator at FR3 frequencies [21], [22].

### C. Contributions

Against the given background and related work, the main contributions of this work are as follows:

1. **A novel dual-components ISAC GBSM framework:** Based on 3GPP recommendations [4], we propose an ISAC channel that consists of a target channel and a background channel. The target channel explicitly models the bistatic propagation path via a sensing target, characterized by its RCS and scattering points (SPs), while the background channel encapsulates non-target propagation.
2. **A hybrid clustering methodology:** To bridge the gap between legacy stochastic models and the geometric fidelity required for sensing, we introduce a novel hybrid stochastic-deterministic clustering approach. Our model augments the standard stochastic clusters from TR38.901 [3] with geometrically defined deterministic clusters that exhibit strict spatiotemporal consistency and absolute delay alignment. This hybrid framework enables a full CIR characterization for all propagation paths including LoS and NLoS components within both the background channel

and the target channel, thereby ensuring critical properties for sensing, such as channel reciprocity.

3. **Comprehensive support for all bistatic modes and propagation conditions:** The proposed framework is designed to support all four fundamental bistatic ISAC configurations defined by 3GPP (transmission reception point (TRP)-TRP, TRP-user equipment (UE), UE-TRP, UE-UE) by introducing the respective mobility scenarios. Furthermore, unlike the existing studies, such as [12], [13], the proposed model explicitly provides the channel coefficients (CC) for all the possible propagation conditions of LoS and NLoS states for transmitter (Tx)-target and target-receiver (Rx) links.
4. **Unified performance validation demonstrating dual-functionality:** Our proposed model is validated through simulations across standardized Urban Macro (UMa), Urban Micro (UMi), and Indoor Factory (InF) scenarios and is further corroborated by real-world channel measurements. This validation demonstrates that the proposed framework maintains full compatibility with TR38.901 [3] for communication performance while simultaneously enabling accurate sensing performance evaluation.

### D. Notation

Unless otherwise mentioned, this paper adheres to the following notational conventions. Scalars are represented by italic letters, e.g.,  $N$ ,  $\sigma$ ,  $\kappa$ , while vectors and matrices are denoted by boldface uppercase and boldface uppercase calligraphic letters, respectively. The transpose, Euclidean norm, and Hermitian norm are denoted by  $(\cdot)^T$ ,  $\|\cdot\|$ , and  $\|\cdot\|_2^2$ , respectively. The magnitude and dot product are expressed as  $|\cdot|$  and  $(\cdot, \cdot)$ . The imaginary unit is defined as  $j \triangleq \sqrt{-1}$ , and the Dirac delta function is  $\delta(\cdot)$ .

### E. Organization

The remainder of this paper is organized as follows. Section II details the proposed geometry-based ISAC channel model. Section III presents the comprehensive framework for bistatic ISAC CM, outlining the procedural steps for generating general parameters, small-scale parameters, and CC. Section IV provides performance evaluation, analyzing communication metrics such as bit-error rate (BER) and ergodic channel capacity, and assessing sensing performance through target ranging accuracy and receiver operating characteristic (ROC) curves. Finally, Section V concludes the paper and suggests directions for future research.

## II. MODELING OF COMPONENTS OF ISAC CHANNEL

As agreed by 3GPP [4], the ISAC CC between  $u$ th Rx antenna element and  $s$ th Tx antenna element,  $\mathcal{H}_{u,s}^{\text{ISAC}}(t, \tau)$  consists of: (1) the target channel,  $\mathcal{H}_{u,s}^{\text{tar}}(t, \tau)$  and (2) the background channel,  $\mathcal{H}_{u,s}^{\text{back}}(t, \tau)$ , where  $t$  is the time snapshot and  $\tau$  is the delay.  $\mathcal{H}_{u,s}^{\text{tar}}(t, \tau)$  comprises all the channel components interacting with the target. In contrast,  $\mathcal{H}_{u,s}^{\text{back}}(t, \tau)$  accounts for all propagation paths that do not undergo interaction with the target. The ISAC CC is given as [4]:

$$\mathcal{H}_{u,s}^{\text{ISAC}}(t, \tau) = \mathcal{H}_{u,s}^{\text{tar}}(t, \tau) + \mathcal{H}_{u,s}^{\text{back}}(t, \tau). \quad (1)$$

The inherent correlation between the background and target channels arises from their co-propagation through a shared

physical environment, where signals may interact with a common set of scatterers.

### A. Target Characterization and Channel Modeling

#### 1) Target Characterization

In ISAC, a target is an object intended for detection, localization, or tracking. Depending on the application, targets can be vehicles, unmanned aerial vehicles (UAVs), or other objects of interest. A target is characterized by its RCS, denoted by  $\sigma$ , which quantifies its scattering behavior and the power reflected toward the sensing Rx. Targets are typically modeled as either a *point target* or an *extended target*. An extended target comprises multiple distributed SPs, resulting in an aggregate return signal that is a superposition of contributions from its individual scatterers, unlike the single dominant reflection from a point target. It is important to note that, unlike TR38.901 [3], in which all clusters are modeled stochastically, we introduce additional deterministic clusters corresponding to the target channel. This allows us to model the target as a separate, controllable component in the ISAC channel simulations, enabling localization in addition to sensing. In fact, besides only detecting targets, the sensed targets/scatterers become resources for communications, namely ISAC sensing identifies the angular positions and relative strengths of key multipath components, which can then be leveraged for power combining over different angular paths, closely related to early work on range extension via multi-path beam combining [23].

In the context of ISAC channel modeling, there are multiple ways target(s) can be modeled in the spatial environment:

##### a) Deterministic Target Placement

A target can be dropped in the Tx-Rx environment by specifying its known 3D Cartesian coordinates  $(x, y, z)$ . Once the coordinates are ascertained, geometric parameters such as the propagation delay, AA, and AD are deterministically derived from the spatial geometry of the Tx, target, and Rx.

##### b) Stochastic Target Placement

Targets can also be modeled by designating a subset of stochastically generated clusters from TR38.901 [3] framework as target clusters. However, these clusters lack geometric consistency as they are not anchored to specific 3D coordinates. To address this, the target cluster's 3D coordinates must be determined post-generation, typically using approaches as in [12], [13], [24]. In III-B, we present a method for deriving the target's 3D coordinates.

#### 2) Environmental Object Characterization and Modeling

EOs also need to be considered for the ISAC CM framework [4]. EOs are non-target objects that have known spatial locations and are categorized by their physical and scattering characteristics relative to the sensing target. Unlike the stochastic cluster, EOs are deterministic positions and scattering properties. Type I EOs exhibit target-like properties, including a defined RCS, velocity profile, and spatially consistent SPs. Type II EOs represent large-scale environmental structures (e.g., buildings, walls) that significantly exceed typical target dimensions and are modeled using the ground-reflection approach in Section 7.6.8 of TR38.901 [3], incorporating specular reflection components as deterministic contributions under NLoS conditions.

TABLE I: Target Channel Propagation Conditions.

Case	Tx-Target	Target-Rx
1	LoS	LoS
2	LoS	NLoS
3	NLoS	LoS
4	NLoS	NLoS

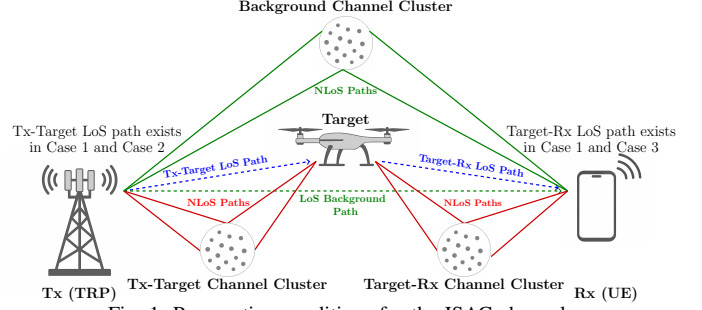


Fig. 1: Propagation conditions for the ISAC channel.

#### 3) Target Channel Modeling

The target channel comprises two cascaded links, that are, the Tx-target link and the target-Rx link. 3GPP TRs, such as TR38.901 [3], TR36.777, TR37.885 serve as a reference to determine the probability of LoS for each link. Furthermore, the target channel LoS/NLoS condition is determined jointly by both constituent links [4]. The target channel is LoS only when both segments are LoS, otherwise, it is NLoS, which results in four possible propagation states for the target channel, as shown in Table I and Fig. 1.

The target channel parameters are generated differently for LoS and NLoS conditions. For LoS target channel, all parameters (AA at the Rx, AD at the Tx, AA and AD at the target, and the propagation delay) are derived deterministically from the Tx-target-Rx geometry. In contrast, for NLoS conditions, we employ a hybrid clustering approach that combines the stochastic and deterministic clusters. Our framework uses deterministic clusters, representing Type I EOs to ensure strict spatiotemporal consistency. These clusters are modeled through geometric computation of all propagation paths (Tx-target, target-Rx, and target-cluster interactions) based on the physical environment's 3D configuration. On the other hand, stochastic clusters serve as an optional addition in NLoS target channel to represent clutter/interference that degrades the sensing performance. The NLoS cluster generation process begins with standard TR38.901 [3] procedures for both links. Subsequently, among the total generated clusters, a subset becomes deterministic clusters with enforced geometric consistency and tailored scattering properties, while the remainder remains stochastic.

The NLoS target channel implementation incorporates absolute propagation delays for both stochastic and deterministic clusters to ensure a physically accurate superposition of all CIR components at the Rx. This requirement arises from the need to preserve correct temporal relationships between paths originating from targets, target channel clusters, and the background channel. The methodology, however, differs between cluster types. For stochastic clusters, absolute delays are generated using the procedural framework defined in TR38.901 [3], Section 7.6.9. In contrast, deterministic clusters possess inherently absolute propagation delays because of geometric consistency, where each path's delay is explicitly

calculated from the positions of the Tx, Rx, and the cluster within a unified coordinate system.

### B. Background Channel Characterization and Modeling

The background channel (as given in Fig. 1) consists of a LoS component, and stochastic NLoS components modeled via cluster-based approach in TR38.901 [3]. As advocated by current ISAC frameworks [4], this methodology provides sufficient characterization of environmental scattering components without requiring precise geometric positioning of clusters. This permits the adoption of the stochastic NLoS CM framework specified in TR38.901 [3] where clusters are represented through statistical parameters, whereby each multipath component is characterized by statistical parameters, e.g., power, delay, Doppler shift, AA & AD. Also, the background channel incorporates absolute delays for NLoS clusters.

## III. BISTATIC ISAC CHANNEL MODELING

The proposed ISAC channel model framework is designed to incorporate the four bistatic sensing modes specified by 3GPP, that are, TRP-TRP, TRP-UE, UE-TRP, and UE-UE [4]. Note that a TRP is a base station (BS). At the most basic level, these four bistatic ISAC sensing modes primarily differ based on the mobility and roles of the Tx and Rx. For instance, the TRP-TRP mode involves two fixed BSs for network-controlled sensing, while the UE-UE mode enables decentralized sensing between mobile devices. A comprehensive framework must therefore be adaptable to these distinct scenarios.

As depicted in Fig. 2, the proposed model follows a structured approach similar to TR38.901 [3], partitioning the modeling process into three core components, that are, (1) the general parameters, (2) small-scale parameters, and (3) coefficient generation. The following sections provide a detailed explanation of each component within our unified ISAC CM framework.

### A. General Parameters

The general parameters define the propagation environment, network configuration, and array characteristics to ensure consistent modeling for both the background and target channels. It begins with selecting a standard scenario (e.g., UMa, UMi, or InF), defining the global and spherical coordinate systems ( $\theta$ ,  $\phi$ ), and specifying scenario-specific sensing requirements. Following this, the network topology and target characteristics are defined, which include: (1) Tx/Rx positions and mobility based on sensing modes, (2) the number of targets,  $L$ , (3) target RCS,  $\sigma$  and the number of SPs,  $K$ , (4) the position vector for  $k$ th SP of  $l$ th target,  $\mathbf{d}_{l,k}$ , where  $l = 1, 2, \dots, L$  and  $k = 1, 2, \dots, K$ , (5) the target velocity (assuming that all the SPs have the same velocity), (6) number of deterministic clusters in Tx-target and target-Rx links, (7) the RCS of the deterministic clusters, and (8) the motion characteristics of the deterministic clusters. The positions of target cluster(s) and deterministic clusters if known or generated randomly, should be explicitly defined. The system center frequency  $f_c$  completes the parameterization.

LoS angles are computed for both the background channel and the target channel considering the Tx, target, and Rx

positions. For the background channel, LoS azimuth angle of arrival (AoA) and zenith angle of arrival (ZoA) at the Rx, i.e.,  $\phi_{\text{LoS,AoA}}$ ,  $\theta_{\text{LoS,ZoA}}$ , azimuth angle of departure (AoD) and zenith angle of departure (ZoD) at the Tx, i.e.,  $\phi_{\text{LoS,AoD}}$ ,  $\theta_{\text{LoS,ZoD}}$ . For the target channel, angles along the Tx-target and target-Rx paths are calculated, which include AoA and ZoA at the Rx and AoD and ZoD at the Tx along the Tx-target and target-Rx links in the target channel, i.e.,  $\phi_{l,k,\text{AoA}}$ ,  $\theta_{l,k,\text{ZoA}}$ ,  $\phi_{l,k,\text{AoD}}$ , and  $\theta_{l,k,\text{ZoD}}$ . This parametrization completes Step 1C and Step 1S.

The background and the target channel propagation conditions (LoS/NLoS) are assigned independently using 3GPP probability models defined in different TRs. The background channel condition (Step 2C) is determined for the Tx-Rx link, while the target channel conditions (Step 2S) are independently evaluated for both Tx-target and target-Rx links [4]. Afterwards, the path loss is obtained for the background channel (Step 3C) and both links in the target channel (Step 3S) using standardized models in TRs. Finally, correlated large-scale parameters, that are, delay spread (DS), angular spread (AS), shadow fading (SF),  $K$ -factor are generated for the background channel (Step 4C) and independently for both Tx-target and target-Rx links (Step 4S).

### B. Small Scale Parameters

The generation of small-scale parameters initiates with Steps 5C and 5S for the background and target channels, respectively, following the TR38.901 [3] procedure to produce relative cluster delays. For the background Tx-Rx link, this yields  $N$  clusters with delays  $\tau'_n$  ( $n = 0, 1, \dots, N-1$ ), where the first cluster represents the LoS path and is set to zero. For the target channel,  $N_1$  and  $N_2$  clusters are independently generated for the Tx-target and target-Rx links, with delays  $\tau'_{n_1}$  ( $n_1 = 0, 1, \dots, N_1-1$ ) and  $\tau'_{n_2}$  ( $n_2 = 0, 1, \dots, N_2-1$ ), respectively, also with their first clusters set to zero.

Here,  $N'_1 = N_1 - 1$  and  $N'_2 = N_2 - 1$ . Subsequently, NLoS clusters are categorized as either deterministic or stochastic. The Tx-target link clusters are divided into  $D_1$  deterministic and  $S_1$  stochastic clusters, while the target-Rx link clusters comprise  $D_2$  deterministic and  $S_2$  stochastic clusters, where  $S_1 = N'_1 - D_1$  and  $S_2 = N'_2 - D_2$ . After extracting the deterministic clusters (indexed  $p_1 = 0, 1, \dots, D_1 - 1$  and  $p_2 = 0, 1, \dots, D_2 - 1$ ), the remaining stochastic clusters are reindexed to  $n_1 = 0, 1, \dots, S_1 - 1$  and  $n_2 = 0, 1, \dots, S_2 - 1$ . This classification is critical as the absolute delay modeling differs between the deterministic and stochastic clusters. It is important to note that the conventional TR38.901 [3] framework defines a methodology for absolute delays but operates primarily on a relative delay basis.

The calculation of absolute propagation delays is critical for ISAC CM. For the background channel, the baseline is established by the LoS delay between the Tx and Rx,  $\tau_{\text{LoS}} = d_{\text{Tx,Rx}}/c$ . The absolute delay for the LoS cluster ( $n = 0$ ) is equal to the baseline delay,  $\tau_0 = \tau_{\text{LoS}}$ . For NLoS clusters ( $n > 0$ ), an excess delay term  $\Delta\tau$  is incorporated, resulting in a total absolute delay of  $\tau_n = \tau'_n + \tau_{\text{LoS}} + \Delta\tau$ . The final ray delays within each cluster, denoted  $\tau_{n,m}$  where  $m = 1, 2, \dots, M$  is the ray index, are generated by applying the intra-cluster delay



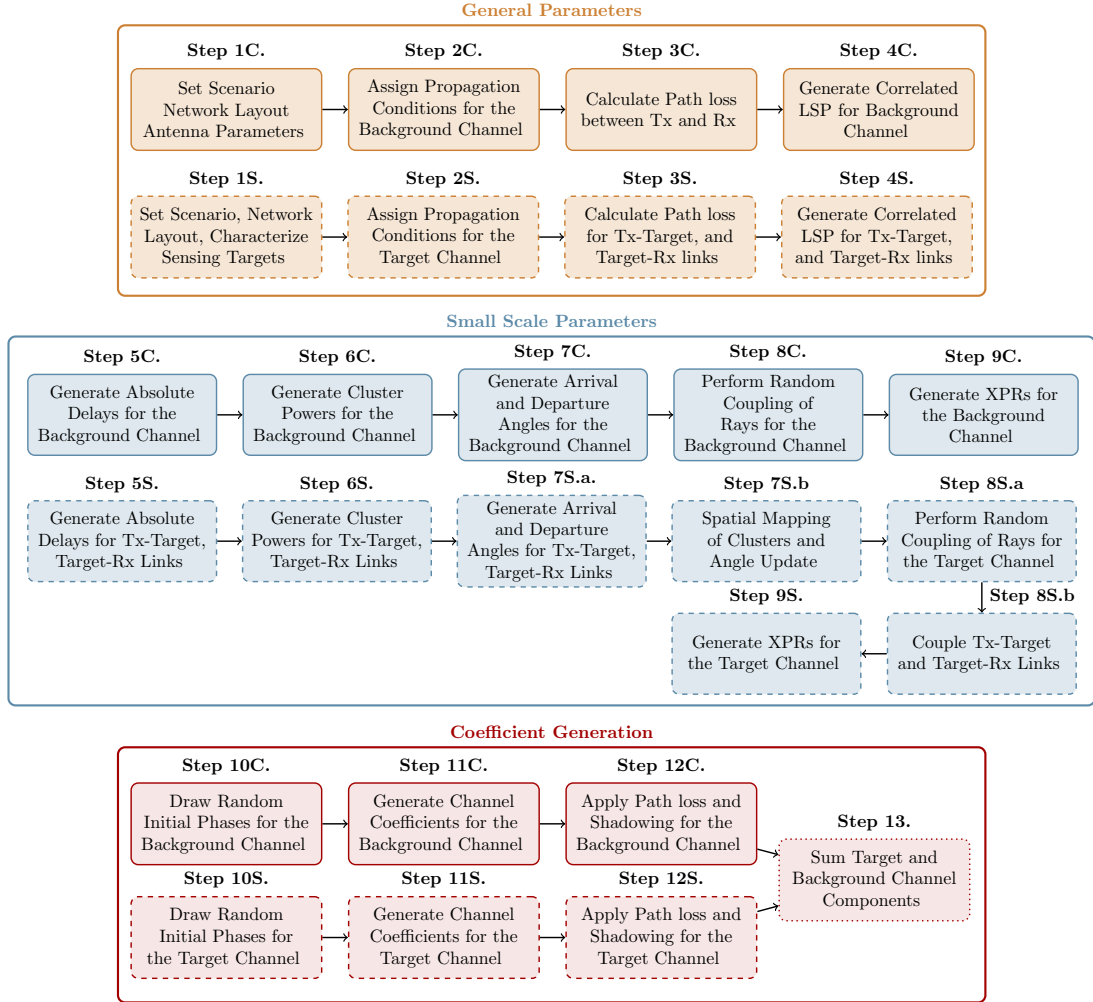


Fig. 2: Proposed bistatic GBSM ISAC CM framework. The processing steps for the background channel are assigned a "C" suffix and are represented by solid-outline rectangles, whereas steps for the target channel use an "S" suffix and are delineated with dashed outlines.

distribution procedure specified in Section 7.6.2.2 of TR38.901 [3] to these absolute cluster delays  $\tau_n$ . Here,  $M$  is the number of rays in a cluster.

In contrast, the target channel requires a separate computation for the Tx-target and target-Rx segments. Each segment has its own LoS baseline, i.e.,  $\tau_{\text{LoS}}^{(1)} = d_{\text{Tx,target}}/c$  for the Tx-target link and  $\tau_{\text{LoS}}^{(2)} = d_{\text{target,Rx}}/c$  for the target-Rx link. These baselines are then combined with cluster-specific delays that differ based on cluster type. Stochastic clusters in the target channel incorporate an excess delay ( $\Delta\tau^{(1)}, \Delta\tau^{(2)}$ ), yielding delays  $\tau_{n_1} = \tau'_{n_1} + \tau_{\text{LoS}}^{(1)} + \Delta\tau^{(1)}$  for the Tx-target link and  $\tau_{n_2} = \tau'_{n_2} + \tau_{\text{LoS}}^{(2)} + \Delta\tau^{(2)}$ . Deterministic clusters, governed by strict geometric consistency, do not require the stochastic excess delay, resulting in geometrically derived delays  $\tau_{p_1} = \tau'_{p_1} + \tau_{\text{LoS}}^{(1)}$  for the Tx-target link and  $\tau_{p_2} = \tau'_{p_2} + \tau_{\text{LoS}}^{(2)}$  for the target-Rx link. Finally, the intra-cluster ray generation procedure is applied, producing the final sets of path delays for the target channel's stochastic ( $\tau_{n_1,m_1}, \tau_{n_2,m_2}$ ) and deterministic ( $\tau_{p_1,k_1}, \tau_{p_2,k_2}$ ) clusters.

Subsequently, cluster powers are generated following the TR38.901 [3] procedure in Steps 6C and 6S. For the background channel, powers  $P_n$  are derived based on the DS,  $\tau'_n$ ,

SF, and  $K^{\text{back}}$ . For the target channel, powers are computed independently for each link, cluster powers  $P_{n_1}$  for the Tx-target link use parameters  $\tau'_{n_1}$ ,  $K_1^{\text{tar}}$ , and corresponding DS and SF values, while powers  $P_{n_2}$  for the target-Rx link use  $\tau'_{n_2}$ ,  $K_2^{\text{tar}}$ , and its associated parameters. Power management employs distinct thresholding strategies; the standard  $-25$  dB threshold from TR38.901 [3] is applied for initial cluster removal in all links, while a relaxed  $-40$  dB threshold as agreed by 3GPP [4] is used during post-concatenation path dropping to accommodate the cascaded nature of bistatic sensing. For ray-level powers, NLoS clusters in the background channel feature equal power distribution among  $M$  rays, yielding  $P_{n,m}$ . The target channel requires distinct treatments, i.e., stochastic clusters generate ray powers  $P_{n_1,m_1}$  and  $P_{n_2,m_2}$  for the Tx-target and target-Rx links, respectively, while deterministic clusters produce SP powers  $P_{p_1,k_1}$  and  $P_{p_2,k_2}$  following a similar procedure as for stochastic clusters.

The AD at the Tx and AA at the Rx for each ray within the NLoS clusters are generated in Step 7C. For the  $m$ th ray in the  $n$ th cluster, the AD at the Tx are characterized by the AoD,  $\phi_{n,m,\text{AoD}}$  and ZoD,  $\theta_{n,m,\text{ZoD}}$ , while the AA at Rx are characterized by the AoA,  $\phi_{n,m,\text{AoA}}$  and ZoA,  $\theta_{n,m,\text{ZoA}}$ .

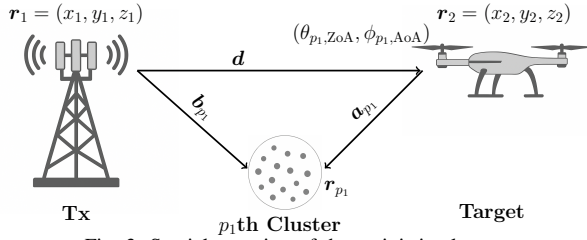


Fig. 3: Spatial mapping of deterministic clusters.

This process follows the TR38.901 [3] methodology, where the AD are statistically generated based on the azimuth spread of departure (ASD) and zenith spread of departure (ZSD), and the AA are generated based on the azimuth spread of arrival (ASA) and zenith spread of arrival (ZSA) obtained for the Tx-Rx link within the background channel.

For the target channel, angles are obtained for both the Tx-target and target-Rx links. In the Tx-target link, the azimuth and zenith AD ( $\phi_{n_1, m_1, \text{AoD}}$ ,  $\theta_{n_1, m_1, \text{ZoD}}$ ) are generated at the Tx, with corresponding AA ( $\phi_{n_1, m_1, \text{AoA}}$ ,  $\theta_{n_1, m_1, \text{ZoA}}$ ) at the target. Similarly, for the target-Rx link, AD ( $\phi_{n_2, m_2, \text{AoD}}$ ,  $\theta_{n_2, m_2, \text{ZoD}}$ ) are generated at the target, with AA ( $\phi_{n_2, m_2, \text{AoA}}$ ,  $\theta_{n_2, m_2, \text{ZoA}}$ ) obtained at the Rx. For deterministic clusters, the corresponding angles are denoted as  $\phi_{p_1, k_1, \text{AoD}}$ ,  $\theta_{p_1, k_1, \text{ZoD}}$ ,  $\phi_{p_1, k_1, \text{AoA}}$ ,  $\theta_{p_1, k_1, \text{ZoA}}$  in the Tx-target link, and  $\phi_{p_2, k_2, \text{AoD}}$ ,  $\theta_{p_2, k_2, \text{ZoD}}$ ,  $\phi_{p_2, k_2, \text{AoA}}$ ,  $\theta_{p_2, k_2, \text{ZoA}}$  in the target-Rx link.

At this stage, only the classification between stochastic and deterministic clusters is complete, while the spatial mapping for deterministic clusters remains unprocessed. For the background channel, Step 8C performs random coupling of rays for both azimuth and zenith angles as defined in TR38.901 [3]. For the target channel, Step 7Sa involves spatial mapping of deterministic clusters, where each cluster (or individual rays within it) are mapped to specific spatiotemporal locations using either AA or AD combined with cluster delay via the law of cosines. When cluster position is determined from one angle set (e.g., AD), the complementary set (AA) must be adjusted to ensure spatiotemporal consistency, realigning them with the determined 3D coordinates, which follows an approach similar to QuadRiGa.

Consider the scenario illustrated in Fig. 3, depicting the  $p_1$ th cluster in the Tx-target link. The Tx and target positions are defined by Cartesian coordinates,  $\mathbf{r}_1$  and  $\mathbf{r}_2$ , respectively, with their separation given by  $\mathbf{d} = \mathbf{r}_2 - \mathbf{r}_1$  and distance  $d = \|\mathbf{d}\|$ . The vector from the Tx to the  $p_1$ th cluster is  $\mathbf{b}_{p_1} = \hat{\mathbf{b}}_{p_1} |\mathbf{b}_{p_1}|$ , where  $\hat{\mathbf{b}}_{p_1}$  is the spherical unit vector and  $|\mathbf{b}_{p_1}|$  is its magnitude. Similarly, the vector from the target to the  $p_1$ th cluster is  $\mathbf{a}_{p_1} = \hat{\mathbf{a}}_{p_1} |\mathbf{a}_{p_1}|$ , where  $\hat{\mathbf{a}}_{p_1}$  is the corresponding spherical unit vector and  $|\mathbf{a}_{p_1}|$  is its length. The azimuth and zenith AA at the target for this  $p_1$ th cluster are  $\phi_{p_1, \text{AoA}}$  and  $\theta_{p_1, \text{ZoA}}$ , respectively, and its absolute delay is  $\tau_{p_1}$ . The cluster's distance is derived from the delay as  $d_{p_1} = \tau_{p_1} c$ . The spherical unit vector  $\hat{\mathbf{a}}_{p_1}$  is determined from the arrival angles as  $\hat{\mathbf{a}}_{p_1} = \mathbf{s}(\theta_{p_1, \text{ZoA}}, \phi_{p_1, \text{AoA}})$ . Applying the law of cosines, the magnitude  $|\mathbf{a}_{p_1}|$  is computed as  $|\mathbf{a}_{p_1}| = \frac{d_{p_1}^2 - d^2}{2(d_{p_1} - d^T \hat{\mathbf{a}}_{p_1})}$ .

Finally, the cluster's spatial coordinates are obtained as  $\mathbf{r}_{p_1} = \mathbf{r}_2 + \hat{\mathbf{a}}_{p_1} |\mathbf{a}_{p_1}|$ . With the 3D coordinates of the  $p_1$ th cluster now determined, the AD at the Tx are recalculated to ensure geometric consistency with the cluster's exact spatial

position. This adjustment aligns the azimuth ( $\phi_{p_1, \text{AoD}}$ ) and zenith ( $\theta_{p_1, \text{ZoD}}$ ) AD with the derived cluster location. A similar approach can be adopted for the target-Rx link having clusters indexed with  $p_2$ . Moreover, same method can be used to obtain the target position vector if generated through stochastic target placement.

Step 8Sa performs random ray coupling for stochastic clusters in both the Tx-target and target-Rx links, following the TR38.901 [3] methodology. Step 8Sb extends this coupling to include both stochastic and deterministic clusters from both Tx-target and target-Rx links, systematically traversing all possible multipath combinations at the target: (1) LoS-LoS coupling, (2) LoS-NLoS coupling, and (3) NLoS-NLoS coupling. In Step 9C, cross polarization ratios (XPRs), ( $\kappa_{n, m}$ ) are generated per TR38.901 [3]'s statistical procedure. For Step 9S, XPR modeling covers both statistical and deterministic clusters across all Table I propagation cases: (1)  $\kappa_{n_1, m_1, 1}$  (LoS target-Rx/NLoS Tx-target), (2)  $\kappa_{n_1, n_2, m_2}$  (LoS Tx-target/NLoS target-Rx), and (3)  $\kappa_{n_1, m_1, n_2, m_2}$  (NLoS in both links) for statistical clusters, with analogous  $\kappa_{p_1, k_1, 1}$ ,  $\kappa_{1, p_2, k_2}$ , and  $\kappa_{p_1, k_1, p_2, k_2}$  for deterministic cases. Statistical XPRs follow standard stochastic modeling, while deterministic XPRs incorporate EO geometry and material properties.

### C. Coefficient Generation

The initial phase generation follows TR38.901 [3] specifications for both background (Step 10C) and both links in the target channels (Step 10S). For the background channel, each ray  $m$  within cluster  $n$  is assigned four random initial phases  $\Phi_{n, m}^{\text{pol}}$  (where  $\text{pol} \in \{\theta\theta, \theta\phi, \phi\theta, \phi\phi\}$ ) drawn uniformly from  $(-\pi, \pi]$ . The target channel extends this to all propagation conditions with statistical clusters require three phase sets, that are,  $\Phi_{n_1, m_1, 1}^{\text{pol}}$  for NLoS Tx-target/LoS target-Rx,  $\Phi_{1, n_2, m_2}^{\text{pol}}$  for LoS Tx-target/NLoS target-Rx, and  $\Phi_{n_1, m_1, n_2, m_2}^{\text{pol}}$  for NLoS Tx-target/NLoS target-Rx. The deterministic clusters follow an identical structure with  $(p_i, k_i)$  replacing  $(n_i, m_i)$  indices, generating  $\Phi_{p_1, k_1, 1}^{\text{pol}}$ ,  $\Phi_{1, p_2, k_2}^{\text{pol}}$ , and  $\Phi_{p_1, k_1, p_2, k_2}^{\text{pol}}$  for the respective propagation cases.

The ISAC CM procedure progresses to coefficient generation in Step 11C. and Step 11S. In the sequel, we first derive the complex CC for the background channel, and then for the target channel.

#### 1) Background Channel

The background channel models the aggregate of all propagation paths between the Tx and Rx that do not interact with the sensing target. It comprises (i) the LoS path and (ii) stochastic NLoS components. A generalized expression for generating CC is given by:

$$H_{u, s, \mathbf{Q}}^{\zeta}(t) = \Gamma^{\zeta} \mathbf{F}_{\text{rx}, u}^T \left( \Omega_{\text{rx}}^{\zeta} \right) \mathbf{c}^{\zeta} \mathbf{F}_{\text{tx}, s} \left( \Omega_{\text{tx}}^{\zeta} \right) \prod_{i \in \{\text{tx}, \text{rx}\}} \mathcal{L}_i \mathcal{D}_i(t), \quad (2)$$

where  $\zeta = \text{LoS, back}$  for LoS or  $\zeta = \text{NLoS, back}$  for NLoS propagation condition for the background channel.  $\mathbf{Q}$  defines the propagation path index, e.g.  $\mathbf{Q} = \{1\}$  for LoS and  $\mathbf{Q} = \{n, m\}$  for the NLoS condition. The model parameters are defined as follows:  $\Gamma^{\zeta}$  can be the complex channel gain, phase term or combination of both.  $\mathbf{F}_{\text{tx}, s} \left( \Omega_{\text{tx}}^{\zeta} \right)$  and  $\mathbf{F}_{\text{rx}, u} \left( \Omega_{\text{rx}}^{\zeta} \right)$  are the field patterns of the  $s$ th transmit and  $u$ th receive

antenna elements, respectively, evaluated at the AD,  $\Omega_{\text{tx}}^\zeta$  and AA,  $\Omega_{\text{rx}}^\zeta$ . The polarimetric properties are characterized by the cross-polarization matrix (CPM),  $\mathcal{C}^\zeta$ . The spatial location phase term,  $\mathcal{L}_j$  accounts for the phase shift induced by the geometry of the antenna array elements, while the Doppler term,  $\mathcal{D}_i(t)$  models the phase shift resulting from the relative motion of Tx and/or the Rx. The subsequent sections provide explicit definitions for these parameters for LoS and NLoS components. We define the spherical unit direction vector as  $\mathbf{s}(\theta, \phi) = [\sin \theta \cos \phi, \sin \theta \sin \phi, \cos \theta]^\text{T}$ , where  $\theta$  and  $\phi$  are the zenith and azimuth angles, respectively. The velocity vector is  $\mathbf{v}(\mathbf{v}, \theta, \phi) = v\mathbf{s}(\theta, \phi)$ , with  $v$  denoting velocity magnitude.

#### a) LoS Component

The LoS component represents the direct path between the Tx and Rx and is modeled in accordance with TR38.901 [3]. Its CC are derived using eq. (2) by setting  $\mathcal{Q} = \{1\}$  (convention used in TR38.901 [3]) and  $\zeta = \text{LoS, back}$ . For the LoS background channel,  $\Gamma^{\text{LoS, back}}$  represents the phase term which is given as  $\Gamma^{\text{LoS, back}} = \exp(-j2\pi d_{\text{Tx, Rx}}/\lambda_0)$ , where  $\lambda_0$  is the carrier wavelength. The antenna field patterns,  $\mathbf{F}_{\text{tx, s}}$  and  $\mathbf{F}_{\text{rx, u}}$ , are evaluated at  $\Omega_{\text{tx}}^{\text{LoS, back}} = \{\theta_{\text{LoS, ZoD}}, \phi_{\text{LoS, AoD}}\}$  and  $\Omega_{\text{rx}}^{\text{LoS, back}} = \{\theta_{\text{LoS, ZoA}}, \phi_{\text{LoS, AoA}}\}$ . The CPM is given as  $\mathcal{C}^{\text{LoS, back}} = \begin{bmatrix} 1 & 0 \\ 0 & -1 \end{bmatrix}$ . The spatial location phase term for a given antenna element position  $\mathbf{d}$  and unit direction vector  $\hat{\mathbf{r}}$  is defined as  $\mathcal{L}(\hat{\mathbf{r}}, \mathbf{d}) = \exp(j2\pi(\hat{\mathbf{r}}^\text{T} \cdot \mathbf{d})/\lambda_0)$ . Here,  $\mathcal{L}_{\text{tx}} = \mathcal{L}(\hat{\mathbf{r}}_{\text{tx, LoS}}, \mathbf{d}_{\text{tx, s}})$  and  $\mathcal{L}_{\text{rx}} = \mathcal{L}(\hat{\mathbf{r}}_{\text{rx, LoS}}, \mathbf{d}_{\text{rx, u}})$ , where  $\hat{\mathbf{r}}_{\text{tx, LoS}} = \mathbf{s}(\theta_{\text{LoS, ZoD}}, \phi_{\text{LoS, AoD}})$  and  $\hat{\mathbf{r}}_{\text{rx, LoS}} = \mathbf{s}(\theta_{\text{LoS, ZoA}}, \phi_{\text{LoS, AoA}})$ . The Doppler term for a given velocity vector,  $\mathbf{v}$  is defined as  $\mathcal{D}(\hat{\mathbf{r}}, \mathbf{v}, t) = \exp(j2\pi(\hat{\mathbf{r}}^\text{T} \cdot \mathbf{v})t/\lambda_0)$ . For LoS component, we have  $\mathcal{D}_{\text{tx}}(t) = \mathcal{D}(\hat{\mathbf{r}}_{\text{tx, LoS}}, \mathbf{v}_{\text{tx}}, t)$  and  $\mathcal{D}_{\text{rx}}(t) = \mathcal{D}(\hat{\mathbf{r}}_{\text{rx, LoS}}, \mathbf{v}_{\text{rx}}, t)$ . The velocity vectors are  $\mathbf{v}_{\text{tx}} = \mathbf{v}(v_{\text{tx}}, \theta_{\text{tx}}, \phi_{\text{tx}})$  for the Tx and  $\mathbf{v}_{\text{rx}} = \mathbf{v}(v_{\text{rx}}, \theta_{\text{rx}}, \phi_{\text{rx}})$  for the Rx, where  $v_{\text{tx}}$  and  $v_{\text{rx}}$  are the velocity magnitudes, while  $\theta_{\text{tx}}, \phi_{\text{tx}}$  and  $\theta_{\text{rx}}, \phi_{\text{rx}}$  are the zenith and azimuth angles of the travel for Tx and Rx, respectively. Note that the classical TR38.901 [3] does not incorporate the velocity of the Tx as it is assumed to be static. However, for ISAC CM it is mandatory to consider the velocity for the both the Tx and Rx as both can be either the BS or UE.

#### b) NLoS Component

The NLoS component aggregates contributions from multiple stochastic clusters, each comprising several rays, as defined by TR38.901 [3]. The CC for the  $m$ th ray within the  $n$ th cluster is obtained from the generalized structure in eq. (2) with  $\mathcal{Q} = \{n, m\}$  and  $\zeta = \text{NLoS, back}$ . In this case,  $\Gamma^{\text{NLoS, back}}$  is the ray power,  $\sqrt{P_{n, m}}$ . The antenna field patterns are evaluated at ray-specific angles, that are,  $\Omega_{\text{tx}}^{\text{NLoS, back}} = \{\theta_{n, m, \text{ZoD}}, \phi_{n, m, \text{AoD}}\}$  and  $\Omega_{\text{rx}}^{\text{NLoS, back}} = \{\theta_{n, m, \text{ZoA}}, \phi_{n, m, \text{AoA}}\}$ . The CPM is given as  $\mathcal{C}^{\text{NLoS, back}} = \mathcal{C}(\kappa_{n, m}, \Phi_{n, m}^{\text{pol}}) = \begin{bmatrix} \exp(j\Phi_{n, m}^{\theta\theta}) & \sqrt{\kappa_{n, m}^{-1}} \exp(j\Phi_{n, m}^{\theta\phi}) \\ \sqrt{\kappa_{n, m}^{-1}} \exp(j\Phi_{n, m}^{\phi\theta}) & \exp(j\Phi_{n, m}^{\phi\phi}) \end{bmatrix}$ , where  $\kappa_{n, m}$  is the XPR and  $\Phi_{n, m}$  contains random initial phases. The spatial location term for NLoS case uses the same functional form but with ray-dependent unit direction vectors. Thus,

$\mathcal{L}_{\text{tx}} = \mathcal{L}(\hat{\mathbf{r}}_{\text{tx, n, m}}, \mathbf{d}_{\text{tx, s}})$  and  $\mathcal{L}_{\text{rx}} = \mathcal{L}(\hat{\mathbf{r}}_{\text{rx, n, m}}, \mathbf{d}_{\text{rx, u}})$ , where  $\hat{\mathbf{r}}_{\text{tx, n, m}} = \mathbf{s}(\theta_{n, m, \text{ZoD}}, \phi_{n, m, \text{AoD}})$  and  $\hat{\mathbf{r}}_{\text{rx, n, m}} = \mathbf{s}(\theta_{n, m, \text{ZoA}}, \phi_{n, m, \text{AoA}})$ . Similarly, the Doppler terms for the Tx and the Rx are given as  $\mathcal{D}_{\text{tx}}(t) = \mathcal{D}(\hat{\mathbf{r}}_{\text{tx, n, m}}, \mathbf{v}_{\text{tx}}, t)$  and  $\mathcal{D}_{\text{rx}}(t) = \mathcal{D}(\hat{\mathbf{r}}_{\text{rx, n, m}}, \mathbf{v}_{\text{rx}}, t)$ .

The background channel CIR is given as:

$$\mathcal{H}_{u, s}^{\text{back}}(t, \tau) = \gamma \mathbf{H}_{u, s}^{\text{LoS, back}}(t, \tau) + \tilde{\gamma} \mathbf{H}_{u, s}^{\text{NLoS, back}}(t, \tau) \quad (3)$$

where  $\gamma = \sqrt{K^{\text{back}}/K^{\text{back}} + 1}$  and  $\tilde{\gamma} = \sqrt{1/K^{\text{back}} + 1}$  are the Rician  $K$ -factor weights. The LoS component is given as  $\mathbf{H}_{u, s}^{\text{LoS, back}}(t, \tau) = [0, \dots, H_{u, s}^{\text{LoS, back}}(t)\delta(\tau - \tau_{u, s}), \dots, 0]$  and the NLoS component as  $\mathbf{H}_{u, s}^{\text{NLoS, back}}(t, \tau) = \sum_{n=1}^N \sum_{m=1}^M [H_{u, s, n, m}^{\text{NLoS, back}}(t)\delta(\tau - \tau_{n, m})] \forall n, m$ , where  $\tau_{u, s} = \|\mathbf{d}_{\text{tx, u}} - \mathbf{d}_{\text{tx, s}}\|/c$  is the LoS propagation delay between the  $u$ th receive and  $s$ th transmit antennas, and  $\tau_{n, m}$  are the delays for the NLoS components obtained following the procedure in TR 38.901 Section 7.6.2.2. Here, each vector represents the CIR across discrete delay bins, with non-zero elements only at the specific delay taps corresponding to  $\tau_{u, s}$  and  $\tau_{n, m}$ .

#### 2) Target Channel

The target channel's propagation characteristics are governed by the Tx-target and target-Rx link states, as categorized in Table I and illustrated in Fig. 1. LoS condition is established only when both constituent links exhibit LoS propagation; any deviation from this condition in either link results in NLoS condition for the target channel. Moreover, the NLoS condition may arise from either stochastic or deterministic clusters present in either of the two links.

The CC for the target channel between the  $u$ th receive and  $s$ th transmit antenna elements are given by the following generalized expression:

$$\begin{aligned} H_{u, s, \mathcal{Q}}^\zeta(t) &= \Gamma^\zeta \mathbf{F}_{\text{rx, u}}^\text{T} \left( \Omega_{\text{rx}}^\zeta \right) \mathcal{C}^\zeta \mathbf{F}_{\text{tx, s}} \left( \Omega_{\text{tx}}^\zeta \right) \prod_{i \in \{\text{tx, rx}\}} \mathcal{L}_i \prod_{j \in \{\text{tx, rx, clus}\}} \mathcal{D}_j(t), \end{aligned} \quad (4)$$

For the target channel, the Doppler terms,  $\mathcal{D}_j(t)$  encompass all moving entities ( $j \in \{\text{tx, rx, clus}\}$ ). The inclusion of the  $\mathcal{D}_{\text{clus}}$  is critical for modeling the relative motion between the target and the deterministic clusters. Note that the stochastic clusters are modeled as stationary as in TR38.901 [3].

#### a) Case 1: LoS Component

The LoS condition manifests when both the Tx-target and target-Rx links maintain unobstructed propagation paths. This scenario represents a specific instantiation of the generalized model in eq. (4) with  $\mathcal{Q} = \{1, 1\}$  and  $\zeta = \text{LoS, tar}$ . Here,  $\Gamma^{\text{LoS, tar}} = \sqrt{\sigma_{l, k}} \alpha(\tilde{d})$  which incorporates the RCS,  $\sigma_{l, k}$  of the  $k$ th SP of the  $l$ th target and the propagation phase shift,  $\alpha(\tilde{d}) = \exp(-j2\pi \tilde{d}/\lambda_0)$ , where  $\tilde{d} = d_{\text{Tx, tar}} + d_{\text{tar, Rx}}$ . The angular parameters for the antenna field patterns are  $\Omega_{\text{tx}}^{\text{LoS, tar}} = \{\theta_{l, k, \text{ZoD}}, \phi_{l, k, \text{AoD}}\}$  and  $\Omega_{\text{rx}}^{\text{LoS, tar}} = \{\theta_{l, k, \text{ZoA}}, \phi_{l, k, \text{AoA}}\}$ . The CPM is given as  $\mathcal{C}^{\text{LoS, tar}} = \mathcal{C}^{\text{LoS, back}}$ . The Tx spatial phase term is  $\mathcal{L}_{\text{tx}} = \mathcal{L}(\hat{\mathbf{r}}_{\text{tx, l, k}}, \mathbf{d}_{\text{tx, s}})$ , where the unit directional vector,  $\hat{\mathbf{r}}_{\text{tx, l, k}} = \mathbf{s}(\theta_{l, k, \text{ZoD}}, \phi_{l, k, \text{AoD}})$ . The Rx spatial term is  $\mathcal{L}_{\text{rx}} = \mathcal{L}(\hat{\mathbf{r}}_{\text{rx, l, k}}, \mathbf{d}_{\text{rx, u}})$ , with  $\hat{\mathbf{r}}_{\text{rx, l, k}} = \mathbf{s}(\theta_{l, k, \text{ZoA}}, \phi_{l, k, \text{AoA}})$ . The Tx Doppler term,  $\mathcal{D}_{\text{tx}}(t) = \mathcal{D}(\hat{\mathbf{r}}_{\text{tx, l, k}}, \mathbf{v}_{\text{tx, l}}, t)$  employs the relative velocity vector between the Tx and the tar-

get,  $\mathbf{v}_{\text{tx},l} = \mathbf{v}_{\text{tx}} - \mathbf{v}_l$ . The Rx Doppler term,  $\mathcal{D}_{\text{rx}}(t) = \mathcal{D}(\hat{\mathbf{r}}_{\text{rx},l,k}, \mathbf{v}_{\text{rx},l}, t)$  uses the relative velocity,  $\mathbf{v}_{\text{rx},l} = \mathbf{v}_{\text{rx}} - \mathbf{v}_l$  between the target and Rx. For the LoS case, the cluster Doppler term is unity, i.e.,  $\mathcal{D}_{\text{clus}}(t) = 1$  since no deterministic clusters are present in the propagation path. The target velocity vector,  $\mathbf{v}_l = v_l(\theta_l, \phi_l)$  is common to all  $K$  SPs of the  $l$ th target, characterized by speed,  $v_l$  and direction angles,  $\theta_l, \phi_l$ .

In addition to the LoS components, the target channel also has NLoS components. The NLoS target components are characterized by the presence of scattering clusters. These scenarios are classified according to whether the clusters are stochastic or deterministic, and whether they occur in the Tx-target link, target-Rx link, or both. The following sections provide detailed derivations for each distinct NLoS condition.

#### b) Case 2a: Stochastic NLoS Component

This scenario corresponds to a LoS Tx-target link with a NLoS target-Rx link due to stochastic clusters, representing an instantiation of the generalized model in eq. (4) with  $\mathcal{Q} = \{1, n_2, m_2\}$  and  $\zeta = \text{SNLoS1, tar}$ . In this case,  $\Gamma^{\text{SNLoS1, tar}} = \sqrt{\sigma_{l,k} P_{n_2, m_2}}$ , where  $P_{n_2, m_2}$  of the  $m_2$ th ray within the  $n_2$ th stochastic cluster in the target-Rx link. The antenna field patterns are evaluated at  $\Omega_{\text{tx}}^{\text{SNLoS1, tar}} = \{\theta_{l,k}, \text{ZoD}, \phi_{l,k}, \text{AoD}\}$  for the Tx and  $\Omega_{\text{rx}}^{\text{SNLoS1, tar}} = \{\theta_{n_2, m_2}, \text{ZoA}, \phi_{n_2, m_2}, \text{AoA}\}$  for the Rx. The CPM for this case is  $\mathcal{C}^{\text{SNLoS1, tar}} = \mathcal{C}(\kappa_{n_2, m_2}, \Phi_{n_2, m_2}^{\text{pol}})$ . The spatial location phase term for the Tx is  $\mathcal{L}_{\text{tx}} = \mathcal{L}(\hat{\mathbf{r}}_{\text{tx},l,k}, \mathbf{d}_{\text{tx},s})$  with  $\hat{\mathbf{r}}_{\text{tx},l,k} = \mathbf{s}(\theta_{l,k}, \text{ZoD}, \phi_{l,k}, \text{AoD})$ , and for Rx, it is  $\mathcal{L}_{\text{rx}} = \mathcal{L}(\hat{\mathbf{r}}_{\text{rx},n_2, m_2}, \mathbf{d}_{\text{rx},u})$ , where  $\hat{\mathbf{r}}_{\text{rx},n_2, m_2} = \mathbf{s}(\theta_{n_2, m_2}, \text{ZoA}, \phi_{n_2, m_2}, \text{AoA})$ . The Tx Doppler term is  $\mathcal{D}_{\text{tx}}(t) = \mathcal{D}(\hat{\mathbf{r}}_{\text{tx},l,k}, \mathbf{v}_{\text{tx},l}, t)$  and the Rx Doppler term is  $\mathcal{D}_{\text{rx}}(t) = \mathcal{D}(\hat{\mathbf{r}}_{\text{rx},n_2, m_2}, \mathbf{v}_{\text{rx}}, t)$ . The cluster Doppler term,  $\mathcal{D}_{\text{clus}}(t) = \mathcal{D}(\hat{\mathbf{r}}_{l, n_2, m_2}, \mathbf{v}_l, t)$  incorporates the target's motion relative to the stochastic cluster, where  $\hat{\mathbf{r}}_{l, n_2, m_2} = \mathbf{s}(\theta_{n_2, m_2}, \text{ZoD}, \phi_{n_2, m_2}, \text{AoD})$ .

#### c) Case 2b: Deterministic NLoS Component

This scenario features a LoS Tx-target link with a NLoS target-Rx link due to deterministic clusters, corresponding to the generalized model in (4) with  $\mathcal{Q} = \{1, p_2, k_2\}$  and  $\zeta = \text{DNLoS1, tar}$ . The CC integrate the LoS component from the Tx-target link with multipath components from deterministic clusters in the target-Rx link. For this scenario,  $\Gamma^{\text{DNLoS1, tar}} = \sqrt{\sigma_{l,k} \sigma_{p_2, k_2} P_{p_2, k_2}}$ , which incorporates the RCS of the deterministic clusters,  $\sigma_{p_2, k_2}$ , along with the SP power,  $P_{p_2, k_2}$ . The antenna field patterns are defined at the angular parameters given as  $\Omega_{\text{tx}}^{\text{DNLoS1, tar}} = \{\theta_{l,k}, \text{ZoD}, \phi_{l,k}, \text{AoD}\}$  and  $\Omega_{\text{rx}}^{\text{DNLoS1, tar}} = \{\theta_{p_2, k_2}, \text{ZoA}, \phi_{p_2, k_2}, \text{AoA}\}$ . The CPM is given as  $\mathcal{C}^{\text{DNLoS1, tar}} = \mathcal{C}(\kappa_{p_2, k_2}, \Phi_{p_2, k_2}^{\text{pol}})$ . Moreover,  $\mathcal{L}_{\text{tx}} = \mathcal{L}(\hat{\mathbf{r}}_{\text{tx},l,k}, \mathbf{d}_{\text{tx},s})$ , and  $\mathcal{L}_{\text{rx}} = \mathcal{L}(\hat{\mathbf{r}}_{\text{rx},p_2, k_2}, \mathbf{d}_{\text{rx},u})$  using  $\hat{\mathbf{r}}_{\text{rx},p_2, k_2} = \mathbf{s}(\theta_{p_2, k_2}, \text{ZoA}, \phi_{p_2, k_2}, \text{AoA})$ . Furthermore, the Tx Doppler term is  $\mathcal{D}_{\text{tx}}(t) = \mathcal{D}(\hat{\mathbf{r}}_{\text{tx},l,k}, \mathbf{v}_{\text{tx},l}, t)$ . The Rx Doppler term,  $\mathcal{D}_{\text{rx}}(t) = \mathcal{D}(\hat{\mathbf{r}}_{\text{rx},p_2, k_2}, \mathbf{v}_{\text{rx},p_2}, t)$ , which employs  $\mathbf{v}_{\text{rx},p_2} = \mathbf{v}_{\text{rx}} - \mathbf{v}_{p_2}$ , capturing the motion between Rx and deterministic clusters. The cluster Doppler term,  $\mathcal{D}_{\text{clus}}(t) = \mathcal{D}(\hat{\mathbf{r}}_{l,k,p_2, k_2}, \mathbf{v}_l, t)$  incorporates  $\mathbf{v}_{l,p_2} = \mathbf{v}_l - \mathbf{v}_{p_2}$ , representing the relative motion between target and deterministic cluster in the target-Rx link, where  $\hat{\mathbf{r}}_{l,k,p_2, k_2} = \mathbf{s}(\theta_{l,k,p_2, k_2}, \text{ZoD}, \phi_{l,k,p_2, k_2}, \text{AoD})$ . The deterministic cluster velocity is characterized by  $\mathbf{v}_{p_2} = \mathbf{v}(v_{p_2}, \theta_{p_2}, \phi_{p_2})$  with speed

$v_{p_2}$  and direction angles  $\theta_{p_2}, \phi_{p_2}$ .

#### d) Case 3a: Stochastic NLoS Component

This scenario features a NLoS Tx-target link with stochastic clusters and a LoS target-Rx link, representing an instantiation of the generalized model in (4) with  $\mathcal{Q} = \{n_1, m_1, 1\}$  and  $\zeta = \text{SNLoS2, tar}$ . The CC integrate stochastic multipath components from the Tx-target link with the LoS component from the target-Rx link. The complex channel gain is defined as  $\Gamma^{\text{SNLoS2, tar}} = \sqrt{\sigma_{l,k} P_{n_1, m_1}}$ , where  $P_{n_1, m_1}$  is the power of the  $m_1$ th ray within the  $n_1$ th stochastic cluster. Moreover,  $\Omega_{\text{tx}}^{\text{SNLoS2, tar}} = \{\theta_{n_1, m_1}, \text{ZoD}, \phi_{n_1, m_1}, \text{AoD}\}$  and  $\Omega_{\text{rx}}^{\text{SNLoS2, tar}} = \{\theta_{l,k}, \text{ZoA}, \phi_{l,k}, \text{AoA}\}$ . The CPM is given as  $\mathcal{C}^{\text{SNLoS2, tar}} = \mathcal{C}(\kappa_{n_1, m_1}, \Phi_{n_1, m_1}^{\text{pol}})$ . Furthermore,  $\mathcal{L}_{\text{tx}} = \mathcal{L}(\hat{\mathbf{r}}_{\text{tx},n_1, m_1}, \mathbf{d}_{\text{tx},s})$ , where  $\hat{\mathbf{r}}_{\text{tx},n_1, m_1} = \mathbf{s}(\theta_{n_1, m_1}, \text{ZoD}, \phi_{n_1, m_1}, \text{AoD})$ , and  $\mathcal{L}_{\text{rx}} = \mathcal{L}(\hat{\mathbf{r}}_{\text{rx},l,k}, \mathbf{d}_{\text{rx},u})$ . The Tx Doppler term is  $\mathcal{D}_{\text{tx}}(t) = \mathcal{D}(\hat{\mathbf{r}}_{\text{tx},n_1, m_1}, \mathbf{v}_{\text{tx}}, t)$  and the Rx Doppler term is  $\mathcal{D}_{\text{rx}}(t) = \mathcal{D}(\hat{\mathbf{r}}_{\text{rx},l,k}, \mathbf{v}_{\text{rx},l}, t)$ . The cluster Doppler term,  $\mathcal{D}_{\text{clus}}(t) = \mathcal{D}(\hat{\mathbf{r}}_{l,n_1, m_1}, \mathbf{v}_l, t)$  incorporates the target's motion relative to the cluster, where  $\hat{\mathbf{r}}_{l,n_1, m_1} = \mathbf{s}(\theta_{n_1, m_1}, \text{ZoA}, \phi_{n_1, m_1}, \text{AoA})$ .

#### e) Case 3b: Deterministic NLoS Component

This scenario features a NLoS Tx-target link due to deterministic clusters and a LoS target-Rx link, corresponding to the generalized model in eq. (4) with  $\mathcal{Q} = \{p_1, k_1, 1\}$  and  $\zeta = \text{DNLoS2, tar}$ . The CC combine multipath components from deterministic clusters in the Tx-target link with the LoS component in the target-Rx link. In this propagation scenario,  $\Gamma^{\text{DNLoS2, tar}} = \sqrt{\sigma_{l,k} \sigma_{p_1, k_1} P_{p_1, k_1}}$ , where  $\sigma_{p_1, k_1}$  is the RCS of the deterministic cluster and  $P_{p_1, k_1}$  is the power of a given SP in the deterministic cluster. The angular parameters are  $\Omega_{\text{tx}}^{\text{DNLoS2, tar}} = \{\theta_{p_1, k_1}, \text{ZoD}, \phi_{p_1, k_1}, \text{AoD}\}$  and  $\Omega_{\text{rx}}^{\text{DNLoS2, tar}} = \{\theta_{l,k}, \text{ZoA}, \phi_{l,k}, \text{AoA}\}$ . The CPM for this propagation scenario is given as  $\mathcal{C}^{\text{DNLoS2, tar}} = \mathcal{C}(\kappa_{p_1, k_1}, \Phi_{p_1, k_1}^{\text{pol}})$ . The spatial location terms are  $\mathcal{L}_{\text{tx}} = \mathcal{L}(\hat{\mathbf{r}}_{\text{tx},p_1, k_1}, \mathbf{d}_{\text{tx},s})$  with  $\hat{\mathbf{r}}_{\text{tx},p_1, k_1} = \mathbf{s}(\theta_{p_1, k_1}, \text{ZoD}, \phi_{p_1, k_1}, \text{AoD})$ , and  $\mathcal{L}_{\text{rx}} = \mathcal{L}(\hat{\mathbf{r}}_{\text{rx},l,k}, \mathbf{d}_{\text{rx},u})$ , where  $\hat{\mathbf{r}}_{\text{rx},l,k} = \mathbf{s}(\theta_{l,k}, \text{ZoA}, \phi_{l,k}, \text{AoA})$ . The Tx Doppler term is  $\mathcal{D}_{\text{tx}}(t) = \mathcal{D}(\hat{\mathbf{r}}_{\text{tx},p_1, k_1}, \mathbf{v}_{\text{tx},p_1}, t)$  which employs the relative velocity  $\mathbf{v}_{\text{tx},p_1} = \mathbf{v}_{\text{tx}} - \mathbf{v}_{p_1}$  between Tx and deterministic cluster, whereas, the Rx Doppler term is  $\mathcal{D}_{\text{rx}}(t) = \mathcal{D}(\hat{\mathbf{r}}_{\text{rx},l,k}, \mathbf{v}_{\text{rx},l}, t)$ . The cluster Doppler term,  $\mathcal{D}_{\text{clus}}(t) = \mathcal{D}(\hat{\mathbf{r}}_{l,k,p_1, k_1}, \mathbf{v}_l, t)$  incorporates  $\mathbf{v}_{l,p_1} = \mathbf{v}_l - \mathbf{v}_{p_1}$ , representing the relative motion between target and deterministic cluster, where  $\hat{\mathbf{r}}_{l,k,p_1, k_1} = \mathbf{s}(\theta_{l,k,p_1, k_1}, \text{ZoA}, \phi_{l,k,p_1, k_1}, \text{AoA})$ . The deterministic cluster velocity is characterized by  $\mathbf{v}_{p_1} = \mathbf{v}(v_{p_1}, \theta_{p_1}, \phi_{p_1})$  with speed  $v_{p_1}$  and direction angles  $\theta_{p_1}, \phi_{p_1}$ .

#### f) Case 4a: Stochastic NLoS Component

This scenario represents a propagation environment where both the Tx-target and target-Rx links experience NLoS conditions due to stochastic clusters. Instantiated from the generalized model in eq. (4) with  $\mathcal{Q} = \{n_1, m_1, n_2, m_2\}$  and  $\zeta = \text{SNLoS3, tar}$ . The complex channel gain is  $\Gamma^{\text{SNLoS3, tar}} = \sqrt{\sigma_{l,k} P_{n_1, m_1} P_{n_2, m_2}}$ . The angular parameters are given as  $\Omega_{\text{tx}}^{\text{SNLoS3, tar}} = \{\theta_{n_1, m_1}, \text{ZoD}, \phi_{n_1, m_1}, \text{AoD}\}$  and  $\Omega_{\text{rx}}^{\text{SNLoS3, tar}} = \{\theta_{n_2, m_2}, \text{ZoA}, \phi_{n_2, m_2}, \text{AoA}\}$ . Moreover, the CPM is given as  $\mathcal{C}^{\text{SNLoS3, tar}} = \mathcal{C}(\kappa_{n_1, m_1, n_2, m_2}, \Phi_{n_1, m_1, n_2, m_2}^{\text{pol}})$ . The spatial location term for the Tx is  $\mathcal{L}_{\text{tx}} = \mathcal{L}(\hat{\mathbf{r}}_{\text{tx},n_1, m_1}, \mathbf{d}_{\text{tx},s})$ . Similarly, the Rx spatial location term is  $\mathcal{L}_{\text{rx}} = \mathcal{L}(\hat{\mathbf{r}}_{\text{rx},n_2, m_2}, \mathbf{d}_{\text{rx},u})$ . The Tx and

Rx Doppler terms are  $\mathcal{D}_{\text{tx}}(t) = \mathcal{D}(\hat{\mathbf{r}}_{\text{tx},n_1,m_1}, \mathbf{v}_{\text{tx}}, t)$  and  $\mathcal{D}_{\text{rx}}(t) = \mathcal{D}(\hat{\mathbf{r}}_{\text{rx},n_2,m_2}, \mathbf{v}_{\text{rx}}, t)$ , respectively. Moreover, the cluster Doppler terms is  $\mathcal{D}_{\text{clus}}(t) = \mathcal{D}(\hat{\mathbf{r}}_{l,n_1,m_1}, \mathbf{v}_l, t)\mathcal{D}(\hat{\mathbf{r}}_{l,n_2,m_2}, \mathbf{v}_l, t)$ .

g) *Case 4b: Deterministic NLoS Component*

This configuration represents the propagation scenario with double-bounce scattering through deterministic clusters in both Tx-target and target-Rx links. Instantiated from eq. (4) with  $\mathcal{Q} = \{p_1, k_1, p_2, k_2\}$  and  $\xi = \text{DNLoS3, tar}$ . For this case,  $\Gamma^{\text{DNLoS3, tar}} = \sqrt{\sigma_{l,k}\sigma_{p_1,k_1}\sigma_{p_2,k_2}P_{p_1,k_1}P_{p_2,k_2}}$ . The angular components are given as  $\Omega_{\text{tx}}^{\text{DNLoS3, tar}} = \{\theta_{p_1,k_1,\text{ZoD}}, \phi_{p_1,k_1,\text{AoD}}\}$  and  $\Omega_{\text{rx}}^{\text{DNLoS3, tar}} = \{\theta_{p_2,k_2,\text{ZoA}}, \phi_{p_2,k_2,\text{AoA}}\}$ . The CPM is  $\mathcal{C}^{\text{DNLoS3, tar}} = \mathcal{C}(\kappa_{p_1,k_1,p_2,k_2}, \Phi_{p_1,k_1,p_2,k_2}^{\text{pol}})$ . The spatial location terms for the Tx and the Rx are given as  $\mathcal{L}_{\text{tx}} = \mathcal{L}(\hat{\mathbf{r}}_{\text{tx},p_1,k_1}, \mathbf{d}_{\text{tx},s})$  and  $\mathcal{L}_{\text{rx}} = \mathcal{L}(\hat{\mathbf{r}}_{\text{rx},p_2,k_2}, \mathbf{d}_{\text{rx},u})$ , respectively. Lastly, the Tx and Rx Doppler terms are given as  $\mathcal{D}_{\text{tx}}(t) = \mathcal{D}(\hat{\mathbf{r}}_{\text{tx},p_1,k_1}, \mathbf{v}_{\text{tx},p_1}, t)$  and  $\mathcal{D}_{\text{rx}}(t) = \mathcal{D}(\hat{\mathbf{r}}_{\text{rx},p_2,k_2}, \mathbf{v}_{\text{rx},p_2}, t)$ , respectively. Furthermore, the cluster Doppler term is  $\mathcal{D}_{\text{clus}}(t) = \mathcal{D}(\hat{\mathbf{r}}_{l,k,p_1,k_1}, \mathbf{v}_{l,p_1}, t)\mathcal{D}(\hat{\mathbf{r}}_{l,k,p_2,k_2}, \mathbf{v}_{l,p_2}, t)$ .

The composite CIR formulations integrate both stochastic and deterministic cluster components across the different propagation scenarios. A generalized expression to obtain the NLoS CIR for the above-mentioned cases is given as:

$$H_{u,s,l,\mathcal{N},\mathcal{P}}^{\text{NLoS}\xi,\text{tar}}(t, \tau) = \sum_k \left( \sum_{\mathbf{m} \in \mathcal{M}_\xi} H_{u,s,\mathbf{Q}}^{\text{SNLoS}\xi,\text{tar}}(t) \delta(\tau - \tau_\xi^S) + \sum_{k \in \mathcal{K}_\xi} H_{u,s,\mathbf{Q}}^{\text{DNLoS}\xi,\text{tar}}(t) \delta(\tau - \tau_\xi^D) \right) \quad (5)$$

where  $\xi \in \{1, 2, 3\}$  denotes the case index,  $\mathcal{N}$  represents the set of stochastic cluster indices,  $\mathcal{P}$  represents the set of deterministic cluster indices,  $\mathbf{Q}$  denotes the ray/cluster index vector,  $\mathcal{M}_\xi$  and  $\mathcal{K}_\xi$  are the summation domains for stochastic and deterministic components in case  $\xi$ , and  $\tau_\xi^S, \tau_\xi^D$  are the corresponding stochastic and deterministic path delays.

The generalized CIR formulation in eq. (5) is instantiated for each specific propagation case through appropriate parameter mappings. For Case 1 ( $\xi = 1$ ), corresponding to LoS Tx-target and NLoS target-Rx propagation, the parameters are specified as  $\mathcal{N} = \{n_2\}$ ,  $\mathcal{P} = \{p_2\}$ ,  $\mathbf{Q} = \{1, n_2, m_2\}$ ,  $\mathcal{M}_1 = \{m_2\}$ ,  $\mathcal{K}_1 = \{k_2\}$ , with delay parameters  $\tau_1^S = \tau_1$  and  $\tau_1^D = \tau_2$ . Here,  $\tau_1 = \tau_{l,s} - \tau_{n_2,m_2}$  represents the net delay through the target and stochastic cluster path, and  $\tau_2 = \tau_{l,k,s} - \tau_{u,l,k,p_2,k_2}$  captures the deterministic path delay via the target's SP and deterministic cluster. The constituent delays include  $\tau_{l,s}$  denoting the propagation delay from the  $s$ th transmit antenna to the  $l$ th target,  $\tau_{n_2,m_2}$  as the delay associated with the  $m_2$ th ray in the  $n_2$ th stochastic cluster, and  $\tau_{u,l,k,p_2,k_2} = (\|\mathbf{d}_{p_2,k_2} - \mathbf{d}_{l,k}\| + \|\mathbf{d}_{\text{rx},u} - \mathbf{d}_{p_2,k_2}\|)/c$  representing the bistatic delay through the deterministic cluster path. For Case 2 ( $\xi = 2$ ), representing NLoS Tx-target and LoS target-Rx propagation, the parameter mappings are  $\mathcal{N} = \{n_1\}$ ,  $\mathcal{P} = \{p_1\}$ ,  $\mathbf{Q} = \{n_1, m_1, 1\}$ ,  $\mathcal{M}_2 = \{m_1\}$ ,  $\mathcal{K}_2 = \{k_1\}$ , with delays  $\tau_2^S = \tau_3$  and  $\tau_2^D = \tau_4$ . The delay parameters are defined as  $\tau_3 = \tau_{n_1,m_1} - \tau_{u,l}$  for the stochastic path and

$\tau_4 = \tau_{s,l,k,p_1,k_1} - \tau_{u,l,k}$  for the deterministic path, where  $\tau_{u,l}$  is the target to Rx delay,  $\tau_{n_1,m_1}$  is the stochastic cluster ray delay,  $\tau_{s,l,k,p_1,k_1} = (\|\mathbf{d}_{p_1,k_1} - \mathbf{d}_{\text{tx},s}\| + \|\mathbf{d}_{l,k} - \mathbf{d}_{p_1,k_1}\|)/c$  represents the Tx to target delay via deterministic cluster, and  $\tau_{u,l,k} = \|\mathbf{d}_{\text{rx},u} - \mathbf{d}_{l,k}\|/c$  is the direct target-Rx path delay. Case 3 ( $\xi = 3$ ) characterizes NLoS propagation in both links and employs the parameter set  $\mathcal{N} = \{n_1, n_2\}$ ,  $\mathcal{P} = \{p_1, p_2\}$ ,  $\mathbf{Q} = \{n_1, m_1, n_2, m_2\}$ ,  $\mathcal{M}_3 = \{(m_1, m_2)\}$ ,  $\mathcal{K}_3 = \{k_1, k_2\}$ , with delays  $\tau_3^S = \tau_5$  and  $\tau_3^D = \tau_6$ , where  $\tau_5 = \tau_{n_1,m_1} - \tau_{n_2,m_2}$  represents the stochastic-stochastic path delay and  $\tau_6 = \tau_{s,l,k,p_1,k_1} - \tau_{u,l,k,p_2,k_2}$  captures the deterministic-deterministic path delay.

The vector CIR components are defined as  $\mathbf{H}_{u,s}^{\text{LoS,tar}}(t, \tau) = [H_{u,s,1,1}^{\text{LoS,tar}}(t) \delta(\tau - \tau_{u,s})] \forall l$ ,  $\mathbf{H}_{u,s}^{\text{NLoS1,tar}}(t, \tau) = [H_{u,s,l,n_2,p_2}^{\text{NLoS1,tar}}(t) \delta(\tau - \tau_1)] \forall l, n_2, p_2$ ,  $\mathbf{H}_{u,s}^{\text{NLoS2,tar}}(t, \tau) = [H_{u,s,l,n_1,p_1}^{\text{NLoS2,tar}}(t) \delta(\tau - \tau_3)] \forall l, n_1, p_1$ , and  $\mathbf{H}_{u,s}^{\text{NLoS3,tar}}(t, \tau) = [H_{u,s,l,n_1,n_2,p_1,p_2}^{\text{NLoS3,tar}}(t) \delta(\tau - \tau_5)] \forall l, n_1, p_1, n_2, p_2$ , where each vector represents the CIR across discrete delay bins, with non-zero elements only at the specific delay taps corresponding to their respective propagation paths.

The target CIR is characterized by distinct formulations determined by the propagation conditions of the constituent Tx-target and target-Rx links. A unified expression encompassing all propagation scenarios is given by:

$$\mathcal{H}_{u,s}^{\text{tar}}(t, \tau) = \gamma_1 \mathbf{H}_{u,s}^{\text{LoS,tar}}(t, \tau) + \gamma_2 \mathbf{H}_{u,s}^{\text{NLoS1,tar}}(t, \tau) + \gamma_3 \mathbf{H}_{u,s}^{\text{NLoS2,tar}}(t, \tau) + \gamma_4 \mathbf{H}_{u,s}^{\text{NLoS3,tar}}(t, \tau), \quad (6)$$

where the weighting coefficients  $\gamma_i$  are configured according to the specific link conditions. The coefficients are derived from the Rician  $K$ -factors of the individual links:  $\eta_1 = \sqrt{K_1^{\text{tar}}/(1 + K_1^{\text{tar}})}$  and  $\eta_2 = \sqrt{K_2^{\text{tar}}/(1 + K_2^{\text{tar}})}$  represent the specular component weights for the Tx-target and target-Rx links respectively, while  $\tilde{\eta}_1 = \sqrt{1/(1 + K_1^{\text{tar}})}$  and  $\tilde{\eta}_2 = \sqrt{1/(1 + K_2^{\text{tar}})}$  correspond to the diffuse component weights.

For LoS propagation, the coefficients are defined as  $\gamma_1 = \eta_1\eta_2$ ,  $\gamma_2 = \eta_1\tilde{\eta}_2$ ,  $\gamma_3 = \tilde{\eta}_1\eta_2$ , and  $\gamma_4 = \tilde{\eta}_1\tilde{\eta}_2$ . When the Tx-target link maintains LoS conditions while the target-Rx link transitions to NLoS propagation, the coefficients are configured as  $\gamma_1 = 0$ ,  $\gamma_2 = \eta_1$ ,  $\gamma_3 = 0$ , and  $\gamma_4 = \tilde{\eta}_2$ . Conversely, for NLoS propagation in the Tx-target link combined with LoS conditions in the target-Rx link, the coefficients become  $\gamma_1 = 0$ ,  $\gamma_2 = 0$ ,  $\gamma_3 = \eta_2$ , and  $\gamma_4 = \tilde{\eta}_1$ . Finally, under NLoS conditions in both links, the channel is characterized by  $\gamma_1 = 0$ ,  $\gamma_2 = 0$ ,  $\gamma_3 = 0$ , and  $\gamma_4 = 1$ .

#### IV. RESULTS, ANALYSIS AND DISCUSSION

In this section, we present a comprehensive evaluation of the proposed ISAC channel, focusing on both communication and sensing performance metrics. The simulations are conducted in 3GPP standardized UMi, UMa, and InF environments. First, we analyze the communication performance by examining the BER of the proposed ISAC channel and comparing it with the classical TR38.901 [3] communication channel model. Additionally, we compare the BER performance in simulated and measured ISAC channels. We also investigate the ergodic channel and analyze the impact of targets with



TABLE II: Parameters used for simulations. In the table, following acronyms are used Orthogonal frequency-division multiplexing (OFDM), Quadrature amplitude modulation (QAM), and uniform rectangular array (URA).

Category	Value/Setting
<b>System Configuration</b>	
Signaling	OFDM
Modulation Scheme	4-QAM
Number of Subcarriers ( $N$ )	256
Length of CP	32
Operating Frequency ( $f_c$ )	7 GHz
Sampling Frequency ( $F_s$ )	100 GHz
<b>Channel &amp; Environment</b>	
Channel Model	Proposed ISAC TR38.901
Scenarios	UMi, UMa, InF
No. of UMi/UMa Clusters	12
No. of InF Clusters	10
No. of Rays per Cluster	20
No. of Deterministic Clusters	5
No. of SPs of Deterministic Clusters	5
<b>Antenna &amp; Mobility</b>	
Tx Configuration	$2 \times 2$ URA $\Rightarrow N_t = 4$
Rx Configuration	$2 \times 2$ URA $\Rightarrow N_r = 4$
Tx Center Coordinates	(0, 0, 5) m
Rx Center Coordinates	(0, 5, 5) m
Tx Velocity	0 m/s
Rx Velocity	0 m/s
<b>Target, Cluster &amp; Clutter Properties</b>	
No. of Targets	1
Target Coordinates	(3, 2, 5) m
Target Velocity	0 m/s
RCS of Target	Varied
No. of SPs of Target	5
RCS of Deterministic Clusters	0.1m <sup>2</sup>
Deterministic Cluster Velocity	0 m/s
InF Clutter Density	10%
InF Clutter Height	2 m

varying RCS. For the sensing performance evaluation, we apply range estimation [25] and detection algorithms [26] and assess their performance through the mean target range error and ROC curves, thereby linking the model to end-to-end detection probability under different target RCS values and distances. Note that the performance of other range estimation and detection algorithms might be different. Unless otherwise explicitly mentioned, the simulation parameters provided in Table II shall be used for the simulations.

#### A. Communication Performance Evaluation

In this section, we evaluate the communication performance for the proposed ISAC channel model, which is benchmarked against the standardized TR38.901 [3] channel [3].

##### 1) BER Analysis in UMi, UMa, and InF Scenarios

Fig. 4(a) presents a comparative analysis of the BER performance between the proposed bistatic ISAC channel model and the conventional TR38.901 [3] channel model. The results obtained considering a target RCS of 0.1m<sup>2</sup> demonstrate near-equivalent performance between both channels, with the proposed ISAC channel exhibiting marginally superior BER. It can be observed that to achieve a BER of 10<sup>-3</sup>, the signal-to-noise ratio (SNR) needed in case of classical TR38.901 InF is 35 dB, whereas, for the proposed model InF, the SNR needed is approximately 34 dB. Similarly, for UMa and UMi of the TR38.901, the SNR required to achieve a BER of 10<sup>-3</sup> is approximately 47.5 dB and 40.5 dB, respectively. For the same BER, the proposed model UMa and UMi scenarios require SNR of 46dB and 40 dB, respectively. This performance enhancement can be attributed to two key factors:

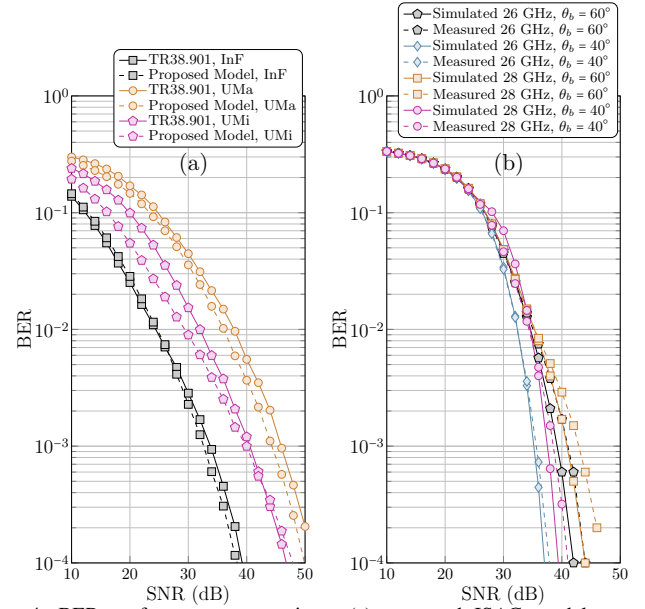


Fig. 4: BER performance comparison: (a) proposed ISAC model versus standard TR38.901 [3] in UMi, UMa, and InF scenarios with a single target (RCS = 0.1 m<sup>2</sup>), (b) proposed model versus measured ISAC channel in an InF scenario under the same target conditions.

(1) the incorporation of target with multiple SPs that introduce additional multipath components, and (2) the presence of deterministic clusters with defined RCS values, as opposed to purely stochastic clusters in TR38.901 [3] communications model. These deterministic clusters provide more structured reflection paths, thereby improving signal reliability. The close alignment in BER performance across different environments affirms that the proposed ISAC channel exhibits similar BER as existing communication standards while simultaneously enabling sensing functionality. Furthermore, the model's adherence to 3GPP parameters ensures seamless integration with current 5G-New Radio (NR) and future 6G systems, making it particularly suitable for applications requiring simultaneous communication and sensing.

##### 2) Comparative BER Performance Analysis: Simulated vs. Measured ISAC Channels

In this section, we present a comparative analysis of the BER performance between the simulated and measured ISAC channels under two distinct bistatic configurations: 40° and 60° as shown in Fig. 4(b). The performance comparison is constrained to a single-input single-output (SISO). For the target characterization, the simulation employs statistical RCS modeling based on empirical measurements [27]. The RCS of the UAV (small-sized) when modeled using log-normal distribution according to 3GPP specifications gives  $A = -13.57\text{dBsm}$ ,  $B_1 = 0\text{dB}$ ,  $B_2 = 3.065\text{dB}$  [27]. The experimental measurements utilize a DJI Mavic 2 Pro UAV with folded dimensions of 214 × 91 × 84mm, unfolded dimensions of 322 × 242 × 84mm, a mass of 907g, and a construction comprising magnesium alloy, reinforced plastic, carbon fiber, glass, and silicon components [27]. The simulated channel considers clutter density of 10% and a clutter height of 2 m to emulate InF propagation conditions.

The experimental measurements were conducted in the KINESIS Lab at NYU Abu Dhabi's Core Technology Platforms,



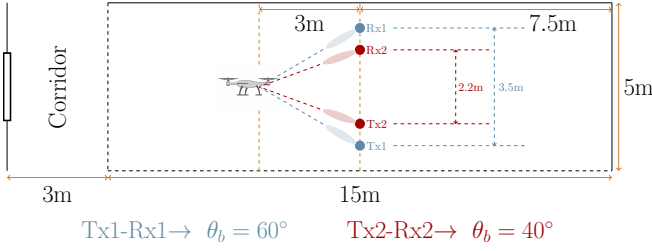


Fig. 5: The layout of the InF measurement environment depicting the Tx-Rx separation for 40° and 60° bistatic configurations.

which emulates InF propagation characteristics. The environment measures 5 m (width)  $\times$  15 m (length)  $\times$  8.5 m (height) and incorporates structural features typical of InF environments, such as high ceilings and open spatial configurations. The experimental setup layout, including the placement of the Tx, Rx, is illustrated in Fig. 5 for both bistatic configurations. To ensure consistency between the simulated and experimental environments, the simulation parameters including the room dimensions and the Tx, Rx, and target coordinates were carefully aligned with the measurement setup. The origin (0,0,0)m was defined at the center of the measurement environment (excluding the corridor), with all positions referenced accordingly. For the 40° bistatic configuration, the Tx, Rx, and target were positioned at (0, -1.1, 1)m, (0, 1.1, 1)m, and (3, 0, 1)m, respectively. In the 60° case, the coordinates were adjusted to (0, -1.75, 1)m (Tx), (0, 1.75, 1)m (Rx), and (3, 0, 1)m (target). The carrier frequencies are set to 26 GHz and 28 GHz and the bandwidth limited to 20 MHz due to the universal software-peripheral radio (USRP) constraints. Moreover, we employ a 2.2 m and 3.5 m Tx-Rx baseline separation  $d_1$ , resulting in bistatic angle of 40° and 60° respectively, at the target coordinates. Both Tx-target and Rx-target distances  $d$  are equal to 3.2 m and 3.5 m for 40° and 60° of bistatic angles respectively as shown in Fig. 5. The bistatic measurement setup configuration and the actual measurement setup indicating a 40° bistatic angle is illustrated in Fig. 6(a) and Fig. 6(b), respectively.

The Tx uses MATLAB-generated Zadoff-Chu sequences of length 128 for waveform generation, upconverted to the 26 GHz and 28 GHz via a Sivers EVK02004 radio-frequency integrated circuit (RFIC) interfaced with a B205mini USRP. The Rx chain performs downconversion and digitization using an identical USRP-RFIC pair. An intermediate frequency of 3 GHz is used at both the Tx and the Rx. During the measurements, both Tx and Rx antennas bore-sight pattern (HPBW = 10° in zenith/azimuth) is carefully aligned to converge at the target's position. It is highlighted that the UAV was rotating around a fixed position to inherently capture the angular effects on the received CIR. Real-time processing is performed to extract CIR from the received waveforms. This experimentally obtained CIR is then employed in simulations where an OFDM waveform (with parameters defined in Table II) is used for BER performance evaluation. All the measurements were conducted in LoS propagation conditions with horizontal polarization for both the Tx and the Rx. The simulated CIR of the proposed ISAC channel is utilized to assess theoretical BER performance.

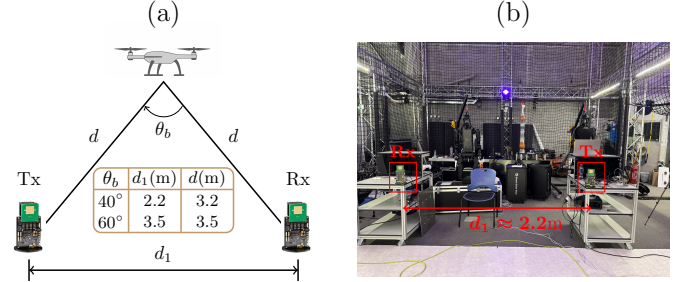


Fig. 6: (a) Bistatic measurement setup configuration, (b) actual measurement setup depicting 40° bistatic arrangement for the Tx and the Rx.

A comparative analysis of the simulated and measured BER performance at carrier frequencies of 26 GHz and 28 GHz, under bistatic angles of 40° and 60°, is presented in Fig. 4(b). The results indicate a consistent behavior across all configurations, wherein the measured ISAC channel exhibits marginally elevated BER relative to its simulated counterpart at high SNR values. For a BER of  $10^{-3}$ , the required SNR was evaluated using both simulated and measured channel models. At a carrier frequency of 26 GHz, the simulated channel requires an SNR of approximately 35 dB and 40.75 dB for bistatic angles of 40° and 60°, respectively. In contrast, when using the measured channel, the required SNRs are 35.5 dB and 37.7 dB for the same angles. At 28 GHz, the required SNR for the simulated channel is 37 dB and 39.5 dB for bistatic angles of 40° and 60°. The corresponding values for the measured channel at this frequency are 37.7 dB and 40.75 dB. This deviation could be attributed to imperfections inherent in measurement setups that are not fully encapsulated within the simulated channel model. Contributing factors include hardware non-idealities, unmodeled propagation effects, subtle calibration inaccuracies, and discrepancies in the RCS between the target used in simulation and the physical UAV employed in measurements.

### 3) Ergodic Channel Capacity and Impact of RCS

In this section, we perform a comparative analysis of the ergodic channel capacity across standardized UMi, UMa, and InF environments considering the proposed ISAC channel and compare it with the standardized TR38.901 [3]. The analysis also quantifies the influence of target RCS on the mean capacity, a critical metric for ISAC system design. The simulation framework, governed by the parameters enumerated in Table II, models a  $4 \times 4$  multiple-input multiple-output (MIMO) link employing OFDM signaling with  $N = 256$  subcarriers. The analysis assumes a normalized noise variance ( $\mu^2 = 1$ ).

Fig. 7 presents a comparative analysis of the mean channel capacity considering the proposed ISAC channel model and the standard TR38.901 [3] channel model for UMi, UMa, and InF scenarios, respectively, evaluated across target RCS values of 0.1m<sup>2</sup>, 0.2m<sup>2</sup>, 0.4m<sup>2</sup>, 0.6m<sup>2</sup>, 0.8m<sup>2</sup>, and 1m<sup>2</sup>. The results indicate that for lower RCS values, e.g., 0.1m<sup>2</sup> and 0.2m<sup>2</sup>, the mean channel capacity across all environments remains nearly identical to the TR38.901 [3] baseline, as the minimal path gain (where the received power is proportional to the target's RCS) results in a negligible contribution to the composite CIR. This small path gain is unable to generate significant additional eigenmodes of the environmental channel matrix, resulting in

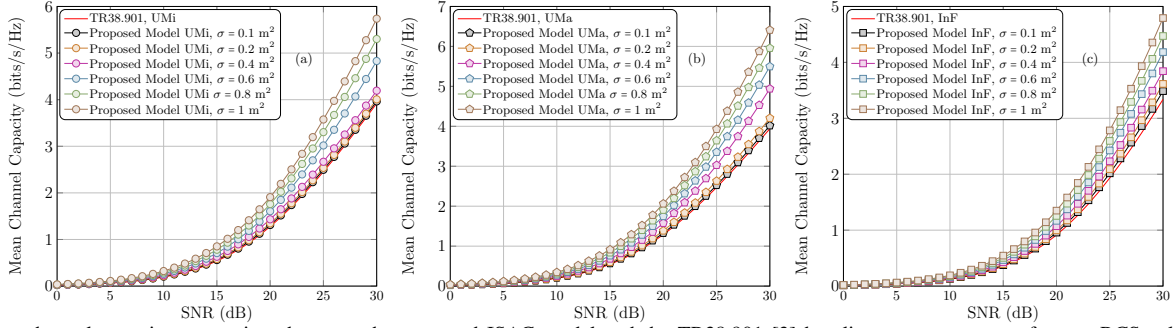


Fig. 7: Mean channel capacity comparison between the proposed ISAC model and the TR38.901 [3] baseline across a range of target RCS values for: (a) UMi, (b) UMa, and (c) InF scenarios.

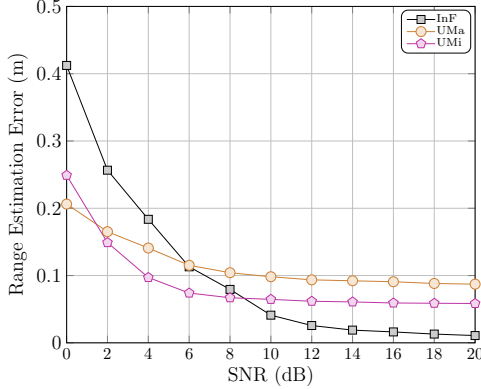


Fig. 8: Target range estimation analysis as a function of SNR for a target with a RCS of  $0.2\text{m}^2$  across UMa, UMi, and InF deployment scenarios.

a minimal increase in the mean channel capacity. Conversely, a high RCS target introduces strong specular reflections that significantly alter the composite CIR resulting in strengthening of dominant eigenmodes, increasing the effective channel rank or increasing the multiplexing gain, thereby directly elevating the mean channel capacity beyond the TR38.901 [3] baseline.

### B. Sensing Performance Evaluation

This section presents performance evaluation of the sensing functionality utilizing the proposed ISAC channel model. The analysis is conducted through a series of Monte Carlo simulations across standardized propagation environments, including UMa, UMi, and InF scenarios. The sensing metrics we consider are target range estimation accuracy and detection performance. The latter is quantified by generating ROC curves, which depict the critical trade-off between the probability of detection ( $P_d$ ) and the probability of false alarm ( $P_{fa}$ ) in different environments.

#### 1) Target Range Estimation

This section evaluates the target range estimation performance using PARAMING algorithm [25] within the proposed ISAC channel model framework. Simulations are conducted across standardized UMa, UMi, and InF deployment scenarios, utilizing the parameter set defined in Table II with a modification that the target RCS is set to  $0.2\text{m}^2$ . The results are depicted in Fig. 8 which indicate that reliable target detection is achievable across all environments, contingent upon sufficient SNR. We observe that the InF scenario achieves higher range estimation accuracy than the UMa and UMi scenarios. This improvement is mainly due to the propagation characteristics

of the InF channel model adopted in our ISAC simulations, which assumes a clutter density of 10% resulting in lower contribution of secondary scatterers, thereby mitigating multipath induced ambiguities and enhancing the reliability of the dominant target echo used for range estimation. Moreover, because of how the radio channel behaves in these environments, i.e., shorter distance, dominant LoS, lower path loss, the UMi scenario gives better performance than the UMa scenario.

Furthermore, as expected due to propagation conditions inherent to the channel, UMi performs better than UMa.

#### 2) Detection Performance via ROC Curves

The following analysis evaluates the detection performance by quantifying the  $P_d$  and  $P_{fa}$ . The evaluation is conducted for two distinct Tx-target-Rx distances,  $d = 27\text{m}$  and  $d = 56\text{m}$ , within standardized UMa, UMi, and InF propagation environments. When  $d = 27\text{m}$ , the Cartesian coordinates for the Tx, target, and Rx are  $(0, 0, 10)\text{m}$ ,  $(0, 5, 10)\text{m}$  and  $(5, 15, 10)\text{m}$ , respectively. On the other hand, for  $d = 56\text{m}$ , the Tx and Rx coordinates remain the same, however, the target is  $(25, 15, 10)\text{m}$ . Moreover, the target RCS we consider are  $0.1\text{m}^2$ ,  $0.5\text{m}^2$  and  $1\text{m}^2$ . The RCS of  $0.1\text{m}^2$  is characteristic of a small-sized UAV, whereas, the RCS of a human adult is approximately  $1\text{m}^2$ . All remaining system parameters are held constant, as specified in Table II. The detection mechanism employs an energy detector [26], which operates on the principle of binary hypothesis testing.

The detection performance, quantified by ROC curves across UMa, UMi, and InF propagation environments, is illustrated in Fig. 9. The results demonstrate an expected dependence on target parameters, i.e., larger RCS values and smaller Tx-target-Rx distances correspond to enhanced detection performance. This improvement is manifested as a higher  $P_d$  for any given  $P_{fa}$ . Conversely, diminished RCS or increased link range reduces the detection probability. The results confirm that target parameters significantly influence sensing reliability in different scenarios. From Fig. 9, we can observe that for  $P_d = 0.9$ , the  $P_{fa}$  in UMa, UMi, and InF is 0.42, 0.4 and 0.44 resp., when  $\sigma = 0.5\text{m}^2$  and  $d = 56\text{m}$ .

### V. CONCLUSIONS

In short, we presented a holistic channel model framework for GBSM bistatic ISAC system. The core contributions are threefold: (1) the introduction of a dual-component ISAC GBSM that explicitly segregates target and background components, enabling concurrent communication and sensing

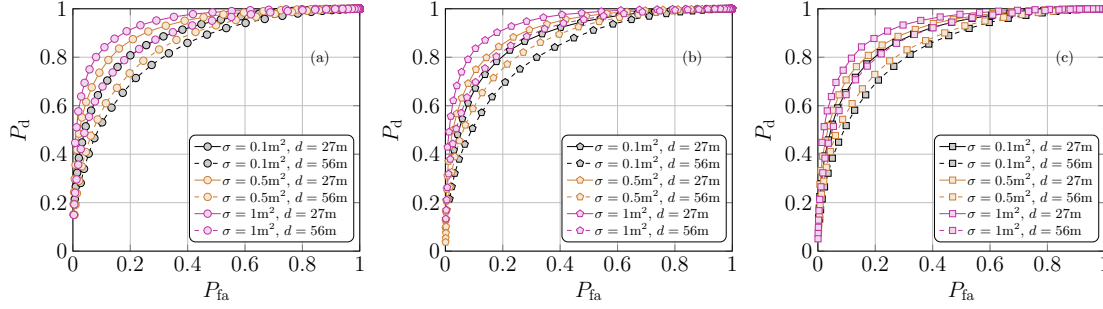


Fig. 9: ROC showing  $P_d$  versus  $P_{fa}$  for (a) UMa, (b) UMi, and (c) InF environments. Each subplot evaluates Tx-target-Rx distances of 27 m and 56 m across target RCS values of 0.1 m<sup>2</sup>, 0.5 m<sup>2</sup>, and 1 m<sup>2</sup>.

performance evaluation, (2) the development of a hybrid clustering methodology that integrates geometrically deterministic clusters with traditional stochastic ones, enforcing the spatiotemporal consistency mandatory for sensing requirements, and (3) a rigorous cross-validation demonstrating that the proposed model retains full backward compatibility with TR38.901 [3] for communication metrics (BER, ergodic capacity) while providing the necessary fidelity to evaluate key sensing performance indicators. The proposed dual-component ISAC GBSM provides an essential foundation for the design, simulation, and validation for future ISAC systems, offering a tool for analyzing the complex interplay and mutual constraints between sensing and communication functionalities in shared channels using an ISAC channel simulator. Our future work will expand the proposed ISAC channel model framework by investigating cluster birth-death dynamics and will also analyze channel non-stationarity under high-velocity and arbitrary trajectory target motion. An important open problem enabled by our framework is the joint identification of target versus background multipath components from measurements. For that, practical algorithms for reliably labeling resolvable paths as "target" or "background" constitute a promising direction for future research.

#### REFERENCES

- [1] R. Liu et al. 'Beginning of the Journey Toward 6G: Vision and Framework'. *IEEE Commun. Mag.*, 61(10):8–9, 2023.
- [2] W. Yang, Y. Chen, N. Cardona, Y. Zhang, Z. Yu, M. Zhang, J. Li, Y. Chen, and P. Zhu. 'Integrated Sensing and Communication Channel Modeling and Measurements: Requirements and Methodologies Toward 6G Standardization'. *IEEE Veh. Technol. Mag.*, 2024.
- [3] 3GPP. 'Study on Channel Model for Frequencies from 0.5 to 100 GHz'. *3GPP, TR38.901, V17.0.0*, April 2022.
- [4] 3GPP TSG RAN WG1. 'Summary on ISAC channel modelling'. R1-2504945, May 2025. TSG RAN WG1 #121, Agenda item 9.7.2, Document for Discussion/Decision.
- [5] H. Wymeersch, N. Tervo, S. Wänstedt, S. Saleh, J. Ahlendorf, O. Akgul, V. Tsekenis, S. Barmounakis, L. Bai, M. Beale, et al. 'Cross-layer Integrated Sensing and Communication: A Joint Industrial and Academic Perspective'. *arXiv preprint arXiv:2505.10933*, 2025.
- [6] 3GPP. 'TR RAN; Spatial channel model for Multiple Input Multiple Output simulations'. TR 25.996, Mar 2020. V16.0.0.
- [7] 3GPP. 'TR RAN; Study on 3D channel model for LTE'. TR 36.873, Oct 2017. V12.7.0.
- [8] S. Nie et al. '72 GHz millimeter wave indoor measurements for wireless and backhaul communications'. *2013 IEEE 24th Annual International Symposium on Personal, Indoor, and Mobile Radio Communications (PIMRC)*, pages 2429–2433, 2013.
- [9] Y. Chen, Z. Yu, J. He, J. Li, and G. Wang. 'A Scatterer-based Hybrid Channel Model for Integrated Sensing and Communications (ISAC)'. In *IEEE PIMRC*, pages 1–7, 2023.
- [10] R. Yang et al. 'A Novel 3D Non-stationary Localization-assisted ISAC Channel Model'. In *IEEE WCNC*, pages 1–6, 2023.
- [11] J. Lou et al. 'A Unified Channel Model for both Communication and Sensing in Integrated Sensing and Communication Systems'. In *IEEE VTC*, pages 1–6, 2023.
- [12] C. Luo, A. Tang, F. Gao, J. Liu, and X. Wang. 'Channel Modeling Framework for Both Communications and Bistatic Sensing Under 3GPP Standard'. *IEEE J. Sel. Areas Sens.*, 2024.
- [13] Q. Ye et al. 'A General Integrated Sensing and Communication Channel Model Combined with Scattering Clusters'. *IEEE Trans. Veh. Technol.*, 2025.
- [14] Y. Liu, J. Zhang, Y. Zhang, H. Gong, T. Jiang, and G. Liu. 'How to Extend 3D GBSM to Integrated Sensing and Communication Channel with Sharing Feature?'. *IEEE Wireless Commun. Lett.*, 2024.
- [15] Z. Zhang, R. He, B. Ai, M. Yang, X. Zhang, R. Chen, H. Zhang, and Z. Zhong. 'A Shared Multipath Components Evolution Model for Integrated Sensing and Communication Channels'. *IEEE Antennas Wireless Propag. Lett.*, 22(12):2975–2978, 2023.
- [16] Y. Chen et al. 'Multi-scattering Centers Extraction and Modeling for ISAC channel Modeling'. In *IEEE EuCAP*, pages 1–5, 2024.
- [17] J. Zhang, J. Wang, Y. Zhang, Y. Liu, Z. Chai, G. Liu, and T. Jiang. 'Integrated Sensing and Communication Channel: Measurements, Characteristics, and Modeling'. *IEEE Commun. Mag.*, 62(6):98–104, 2023.
- [18] O. Kanhere, S. Ju, Y. Xing, and T. S. Rappaport. 'Map-Assisted Millimeter Wave Localization for Accurate Position Location'. In *IEEE GLOBECOM*, pages 1–6. IEEE, 2019.
- [19] A. Bazzi et al. 'ISAC Imaging by Channel State Information using Ray Tracing for Next Generation 6G'. *IEEE J. Sel. Top. Electromagn., Antennas Propag.*, 2025.
- [20] H. Poddar, S. Ju, D. Shakyia, and T. S. Rappaport. 'A tutorial on NYUSIM: Sub-Terahertz and Millimeter-Wave Channel Simulator for 5G, 6G, and Beyond'. *IEEE Communications Surveys & Tutorials*, 26(2):824–857, 2023.
- [21] M. Ying et al. 'Multi-Stage Location Optimization Through Power Delay Profile Alignment Using Site-Specific Wireless Ray Tracing'. pages 1–6, Taipei, Taiwan, December 2025. IEEE.
- [22] M. Ying, D. Shakyia, P. Ma, G. Qian, and T. S. Rappaport. 'Site-Specific Location Calibration and Validation of Ray-Tracing Simulator NYURay at Upper Mid-Band Frequencies'. *npj Wireless Technology*, 2025. invited paper, to appear.
- [23] Shu Sun et al. 'Millimeter wave multi-beam antenna combining for 5G cellular link improvement in New York City'. In *2014 IEEE International Conference on Communications (ICC)*, pages 5468–5473, 2014.
- [24] S. Jaekel et al. 'QuaDRiGa: A 3-D Multi-cell Channel Model with Time Evolution for Enabling Virtual Field Trials'. *IEEE Trans. Antennas Propag.*, 62(6):3242–3256, 2014.
- [25] S. Naoumi, A. Bazzi, R. Bomfin, and M. Chafii. High-Resolution Sensing in Communication-Centric ISAC: Deep Learning and Parametric Methods. *arXiv preprint arXiv:2509.02137*, 2025.
- [26] R. Bomfin and M. Chafii. 'On the Performance Analysis of Zero-Padding OFDM for Monostatic ISAC Systems'. *IEEE Trans. Commun.*, 73(3):2103–2117, 2025.
- [27] A. W. Azim, A. Bazzi, R. Bomfin, and M. Chafii. '3GPP-Compliant Radar Cross Section Characterization of Indoor Factory Targets'. In *IEEE GLOBECOM*, 2025. Accepted for publication.